Angle-Resolved Photoemission Studies on High Temperature Superconductor Bi2Sr2CuO6+[delta]

Author: Zhihui Pan

Persistent link: http://hdl.handle.net/2345/1369

This work is posted on eScholarship@BC,
Boston College University Libraries.

Boston College Electronic Thesis or Dissertation, 2008

Copyright is held by the author, with all rights reserved, unless otherwise noted.

Boston College

The Graduate School of Arts and Sciences

Department of Physics

Angle-Resolved Photoemission Studies on High Temperature Superconductor $\mathbf{Bi_2Sr_2CuO_{6+\delta}}$

a dissertation

by

Zhihui Pan

submitted in partial fulfillment of the requirements

for the degree of

Doctor of Philosophy

September 8, 2008

© **copyright by Zhihui Pan**

2008

Angle-Resolved Photoemission Studies on High Temperature Superconductor $Bi_2Sr_2CuO_{6+\delta}$

Zhihui Pan

Dissertation advisor: Dr. Hong Ding

Abstract

High temperature superconductivity has been one of the most challenging problems in condensed matter physics since its discovery. This dissertation presents systematic studies on electronic structures of single layer high temperature superconductor $Bi_2Sr_2CuO_{6+\delta}$ by angle-resolved photoemission spectroscopy.

A high binding energy band anomaly is observed in $Pb_xBi_{2-x}Sr_2CuO_{6+\delta}$. Comparing with LDA calculation, the band is highly remonetized by a factor of 3, the incoherent part coexists and forms a band anomaly as a non-dispersive dive structure. Systematic studies are performed on $Bi_{2+x}Sr_{2-x}CuO_{6+\delta}$ with a wide doping range, revealing a linear doping nature of Bi substitution. An unusual Coulomb gap is observed in the heavily substituted samples. Our results reveal the dual role of off-plane chemical substitution in high-T_C cuprates and elucidate the nature of the quantum electronic nature due to strong correlation and disorder. High resolution ARPES on $La_xBi_2Sr_{2-x}CuO_{6+\delta}$ observes a large gap and a small gap coexisting at antinodal region below T_C. The small gap is d-wave like and attributed to superconductivity, while the large gap is attributed to a CDW order. A strong short-ranged

correlation between the small and large gap magnitude suggesting that superconductivity and charge ordering are driven by similar physical mechanism.

To my family.

Acknowledgements

First, I would like to thank Professor Hong Ding who has been an exceptional mentor and friend for the last five years. He has taught me not only physics concepts but also many experimental skills. With his enthusiasm, his inspiration, and his great efforts to explain things clearly and simply, he helped to make physics fun for me.

I would like to thank Dr. Alexei V. Fedorov for the guidance and help at Advanced Light Source. It is a great experience working with him on an excellent APRES system at Beamline 12.

I would like to thank Professor Ziqiang Wang and Professor Vidya Madhavan for many beneficial discussions and academic advices. The collaborations with their groups have been very efficient and productive.

I want to thank Shancai Wang and Hongbo Yang, who showed me how to do experiments and data analysis when I entered the group. They are warmhearted friends in SRC and shared night shifts during my first SRC run. I also want to thank my labmates Asoka Kumar, Jihua Ma, Madhab Neupane, Yiming Xu, Pierre Richard, Philopater Bishay for their supports and helps during experiments. I want to thank them for sharing the summer fresh cow smell and the winter snow at SRC.

I want to thank many other faculties and staffs in the Physics department. Their kindness to me has made my stay in Boston College a very pleasant experience.

I would like to thank Professor Takashi Takahashi for his support to doing experiments in his group in Tohoku University. I also want to thank Professor Takafumi Sato, Dr. Seigo Souma, Dr. Hiroaki Matsui, Dr. Kensei Terashima, Kosuke Nakayama, Toshiyuki Arakane for great discussions and help during during the experiments. Their diligence inspired me many times. Here I expressed my gratitude to all the members in their group.

I would like to thank Peter Johnson, Tonica Valla, Tim Kidd and Jon Rameau for the warmhearted help during experiment at Brookhaven National Lab. I also thank Genda Gu for providing us so many high quality single crystals.

I would like to thank Professor Haihu Wen, Huiqian Luo, Lei Fang for providing so many excellent samples. Without those sample, this work could not be done.

I thank all my friends here at Boston for filling my life with happiness.

I thank my wife Jing Wang, knowing she is the best thing that has ever happened to me.

At last, I want to thank my parents. They bore me, raised me, supported me, taught me and loved me. To them I dedicate this thesis.

Contents

Chapter 1

Introduction

1.1 Conventional superconductivity

Superconductivity was first discovered by H. K. Onnes [1] in 1911, when mercury was cooled down to liquid He temperature 4.2K, the electronic resistivity dropped suddenly and became zero. Since then many experiments and theories have been done and proposed to understand this phenomenon and to find superconductors with higher T_C. In the superconducting state, superconductors exhibit two characteristic properties: (1) There is no measurable DC electric resistivity; (2) A superconductor exhibits perfect diamagnetic behavior.

Zero resistivity Resistivity of superconductors drops abruptly to zero when temperature is blow some value. The onset temperature at which resistivity drops abruptly is called the critical temperature T_C. Values of T_C are different from materials to materials, varying from less than 1 K to more than 100 K. Below T_C electric current can persist in a superconductor for years without observable dissipation. For normal metals, resistance can be described by Ohm's law as $R = V/I$. An electrical current is generated when an external electric filed is applied. The current will be dissipated quickly once the external field is removed because of collisions between electrons and lattice ions. During collisions, energies carried by the current will be absorbed by the lattice and converted into heat. This is the electrical resistance. Resistivity of normal metals usually decreases as temperature goes down, but retains a finite value at $T = 0$ K, known as residual resistivity. The finite value of residual resistivity is due to existence of impurities and defects. However the zero resistivity in a superconductor is a really new phenomenon other than a perfect metal.

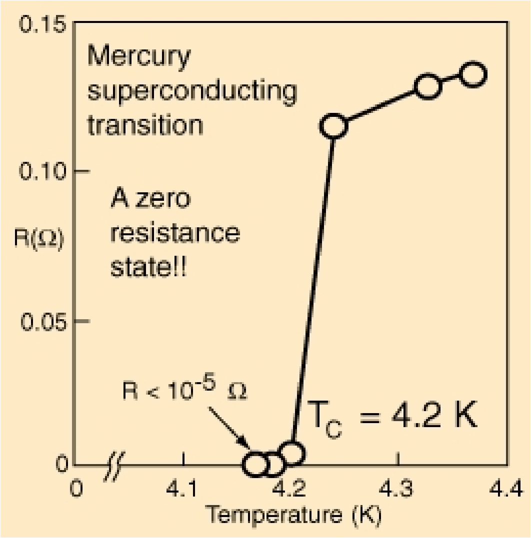

Figure 1.1: Resistivity of mercury.

Meissner effect Another phenomenon characterizing superconductivity is Meissner effect [2], discovered by Meissner in 1933. He found that below T_C, superconductors exhibit perfect diamagnetic. Figure 1.2a shows a schematic Meissner effect. At $T > T_C$, magnetic field can penetrate a sample, when temperature is cooled below T_C, the magnetic field is repelled out of the sample. This can not be explained just by perfect conductivity and is thus a characterized property of superconductivity. Actually as magnetic field increases, superconductivity is suppressed and T_C decreases, a phase diagram can be drawn like Figure 1.2. If the external magnetic field is large enough, superconductivity will be destroyed and the field is called the critical field H_C. With applying external magnetic field, normal state can be achieved below T_C. Without external magnetic filed, when the current is above a certain value, superconductivity will also disappear and the material behaves like a normal metal. This value of

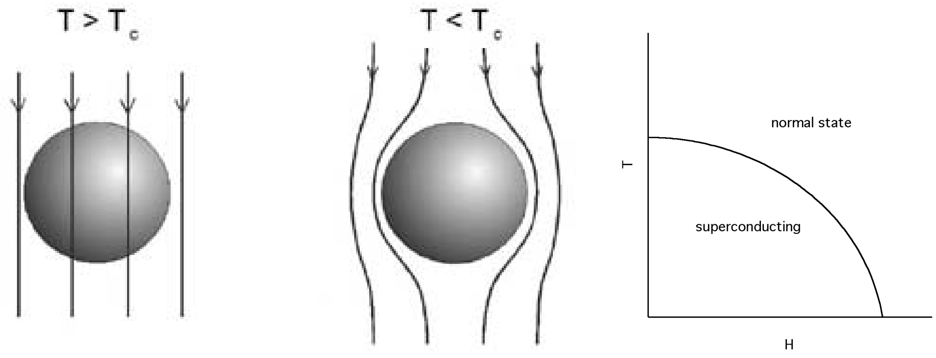

Figure 1.2: Schematic diagram of Meissner effect and phase diagram of in term of temperature and magnetic field. Left panel is the magnetic field above T_C and middle panel shows the magnetic field below T_C

current is called the critical current. The existence of critical current may be related to Meissner effect since the current itself can generate a magnetic field. When the magnetic filed generated by the current reaches H_C, superconductivity is destroyed.

Specific heat anomaly The third phenomenon is the anomaly specific heat at transition temperature. For normal metals, specific heat can be written as $AT + BT^3$, the first term is due to electron-electron interactions and the latter comes from electron-phono interactions. Figure 1.3 shows the temperature dependence of specific heat schematically. With H = 0 T, as T decreases, specific heat jumps up at T_C and then decreases slowly. With a magnetic field, a superconductor can be driven

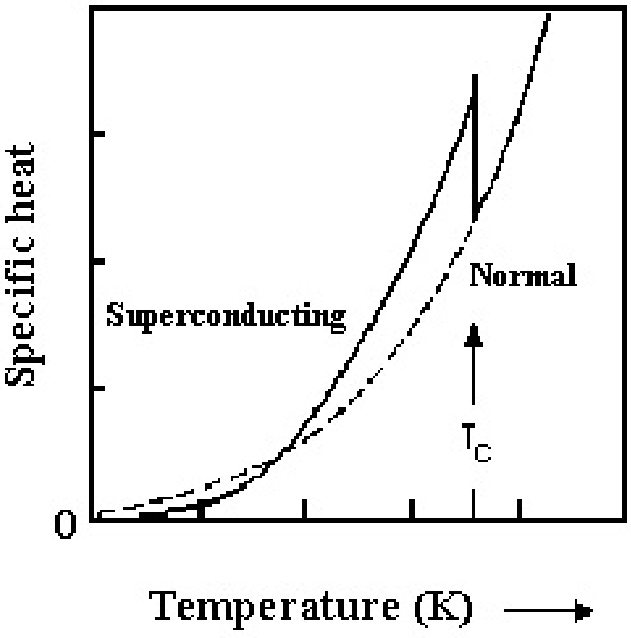

Figure 1.3: Comparison of specific heat in supconducting state and normal state.

into the normal state even at lower temperatures, the specific heat can be compared between the normal state and superconducting state below T_C. One can see clearly just below T_C, the specific heat in superconducting state is higher than the one in the normal state, but at very low temperature, superconducting specific heat becomes lower than the normal state one. The linear term in the specific heat is replaced by a term which drops faster. At very low temperature, the specific heat is dominated by a term $\exp(-\Delta/k_B T)$.

Conventional superconductivity has been a challenging problem since its discovery until 1957 when J. Bardeen, L. N. Copper and J. R. Schreiffer proposed their BCS theory [8]. According BCS theory, superconductivity is generated through electron-phonon interaction. An electron is attracted to an ion through Coulomb interaction. Because the ion mass is much larger than the electron mass, the ion will respond much more slowly compared to electrons. When an electron moves away, before the ions respond, another electron can move into the ionic hole. This provides an effective attractive interaction between two electrons, which will cause tese two electrons to form a so-called Cooper pair. The energy spectrum of a Cooper pair possesses an energy gap, meaning there is a minimum energy that must be supplied in order to excite the pair electrons. If the energy gap is larger than the thermal energy of lattices, then Cooper pairs will not be scattered by the lattice. Cooper pair fluid becomes a superfluid without energy dissipation. The coherence of Cooper pairs drives all paired electrons into a same quantum state, leading to superconductivity. BCS theory can explain many experimental phenomenon observed in superconductors: (1) the s-wave symmetry of the superconducting gap of conventional superconductivity; (2) the specific heat anomaly at T_C and its exponentially suppression at very low temperature. BCS theory correctly explained the Meissner effect.

1.2 High temperature superconductivity

Many efforts have been put into synthesizing superconducting materials with higher T_C, but T_C has been enhanced slowly before 1980s with the highest $T_C = 23$K. High temperature superconductor $\mathrm{La}_{2-x}\mathrm{Ba}_x\mathrm{CuO}_4$ with $T_C \approx 35$K [3] was discovered by J. G. Bednorz and K. A. Müller in 1986. This discovery of $\mathrm{La}_{2-x}\mathrm{Ba}_x\mathrm{CuO}_4$ stimulated a rapid raising of transition temperature, and many high-Tc superconductors have been synthesized. In 1987, T_C was brought above 77K [4], the liquid nitrogen temperature. This is important since liquid nitrogen can be produced relatively easily and cheaply. Now the record of T_C of 138K is held by $\mathrm{Hg}_{0.8}\mathrm{Tl}_{0.2}\mathrm{Ba}_2\mathrm{Ca}_2\mathrm{Cu}_3\mathrm{O}_{8+\delta}$ [5]. The discovery of high-Tc superconductivity in an transition-metal oxide was quite unexpected. High-T_C superconductors exhibit so many unusual phenomena that they likely superconductivity must come from a novel mechanism which is not clear until now. Nevertheless, people have learned many properties of high-T_C superconductors during last 20 years.

- There is a large hole-like Fermi surface in almost all high-T_C superconductors.

- High-T_C superconductors have an anisotropic d-wave symmetry order parameter.
- There is a pseudogap phase in underdoped region.
- Superconductivity happens at the Cu-O planes.
- Lack of isotope effect, especially in optimally doped high-T_C superconductors.
- Type II superconductor with high $H_c(\sim 100T)$
- Parent compound is antiferromagnetic insulator.
- Layered crystal structure, with T_C enhanced as the number of Cu-O layers in one unit cell increases (up to 3 layers).
- There is a dispersion anomaly or kink at a relatively high energy (40 $\sim$ 70 meV).

Crystal structure All the high-T_C superconductors share the two-dimensional CuO_2 planes separated by other blocks, some of them known as charge reservoir, which will (1)dope carriers into the CuO_2 plane and (2) separate the CuO_2 planes so that the coupling between them is weak and cause the system to be 2-dimensional system. Take LSCO as an example, which has the same structure as LBCO. The crystal has I4/mmm symmetry, with the lattice constants a=b=3.78 Å, c=13.25 Å. Cu and O atoms form CuO_2 planes, which are well separated by two LaO planes. This make the electronic structure more two-dimensional like and the 2D lattice can be viewed as a square lattice. Superconductors can be classified by the number of CuO_2

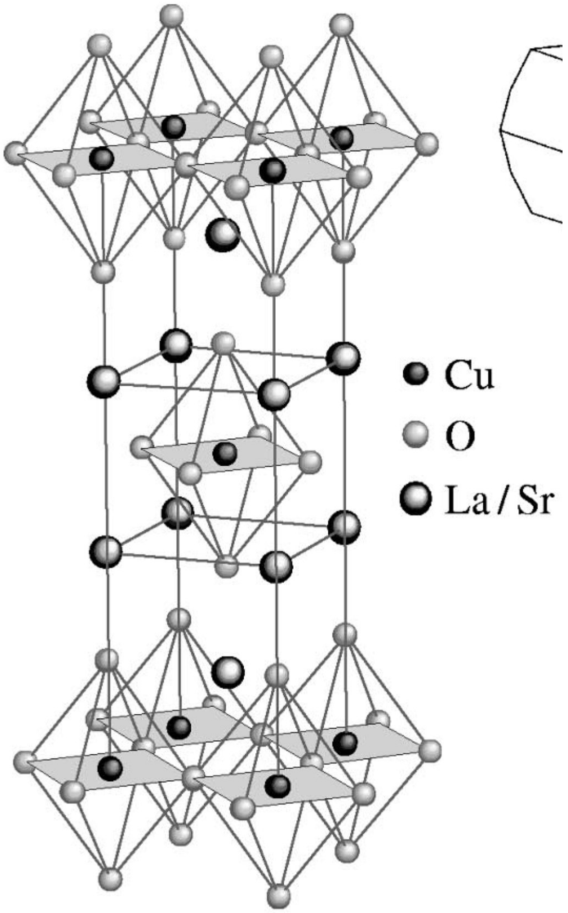

Figure 1.4: Crystal structure of $La_{2-x}Sr_xCuO_4$.

planes in one unit cell: single layer, bilayer, and multilayer families. T_C increases as the number of layers increase until n > 3.

Electronic structure All the high-T_C superconductors share the CuO_2 plane. Soon after the discovery of the high-T_C superconductivity, it was proposed that superconductivity happens in the CuO_2 plane [6]. The high-T_C cuprates exhibit a quasi-2D electronic structure with weak c direction band dispersion. So the electronic structure can be discussed in two dimensional k-space and the 3D Brillouin zone can be also projected into a square. In a parent compound like La_2CuO_4, Cu atom is surrounded by six oxygen atoms which form an octahedral environment. Due to the octahedral crystal filed, the $3d$ states will split into two degenerated states, e_g and t_{2g} states. The distortion due to the shift of the apical oxygens make those states split further. e_g splits into $3d_{x^2-y^2}$ and $3d_{3z^2-r^2}$, t_{2g} splits into $3d_{xy}$, $3d_{xy} and 3d_{yz}$ states. The valence of Cu is 2+ so Cu^{2+} has a $3d^9$ electronic configuration. All the states will be fully occupied except the topmost $3d_{x^2-y^2}$ which is half filled. Due to electron hopping between Cu atom and O atom, Cu $3d_{x^2-y^2}$ will hybridize with the O $2p$ states and thus the electronic structure can be described by a three-band model. The anti-bonding band is at the Fermi level, the nonbonding and bonding bands are at higher binding energy levels. The Cu $3d_{x^2-y^2}$ orbital is singly occupied while the O $2p$ orbitals are doubly occupied, the hopping between Cu and O is t_{pd}. There is a strong Coulomb repulsion energy U_d for doubly occupied Cu d electrons, which is much larger than the nearest hopping energy. In the one band Mott-Hubbard insulator, when the Coulomb

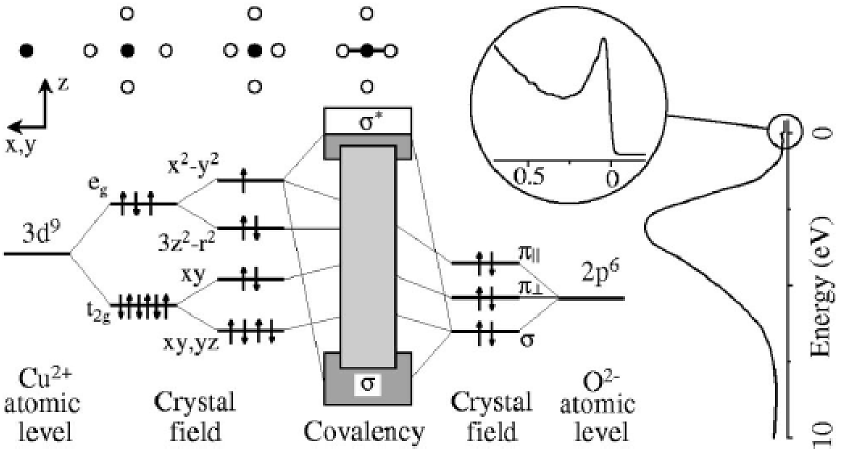

Figure 1.5: Electronic structure of the CuO$_2$. Cu^{2+} has $3d^9$ configuration. Octahedral environment splits Cu 3d orbitals into e_g and t_{2g} states. Distortion of apical oxygens further splits e_g into $3d_{x^2-y^2}$ and $3d_{3z^2-r^2}$, t_{2g} into $3d_{xy}$, $3d_{xy}$ and $3d_{yz}$ states. Cu 3d orbitals form covalence with O 2p orbitals.

repulsion U is larger than the band width W, the band will split into upper Hubbard band(UHB) and lower Hubbard band(LHB). The LHB will be fully filled and UHB will be empty, their energy difference is called Mott gap which can be a few electro-volts, and the system becomes an insulator. In cuprates, the oxygen $2p$ orbitals lie at energy E_p, which is higher than E_d, but $E_p - E_d$ is much smaller than U_d that the charge-transfer excitation from d to p will be the lowest energy excitation as shown in Fig. 1.6. $E_p - E_d$ plays the role of Hubbard U in the one band model of the Mott insulator and the gap between LHB and UHB is called the charge transfer gap Δ. The material becomes insulator because of the opening of a charge transfer gap. Virtual hopping to doubly occupied states leads to an exchange interaction $J\mathbf{S_1} \cdot \mathbf{S_2}$, where $J = t_{pd}^4/(E_p - E_d)^3$. At the half filling, as charge excitations are gapped, Cu becomes antiferromagnetic because both spin can virtually hop to the E_p orbital. In deed, the parent compounds are found to be antiferromagnetic insulators. In terms of hole picture, the Cu 3d orbital is occupied by one hole with spin $S = 1/2$, oxygen orbitals is empty. The carriers on the $\mathrm{CuO_2}$ plane can be changed via chemical substitution, this process is called doping. Doped cuprates can be described by a single-band Hubbard model. Because the E_p is above E_d, so the doped hole will reside on the oxygen site. The doped hole will resonate on the four oxygen atoms surrounding a Cu. The spin of the doped hole combines antiparallel with the spin on the Cu forming a spin singlet, commonly known as Zhang-Rice singlet [17]. So cuprates are described by:

$$H = -\sum_{<i,j>,\sigma} t_{ij} c_{i\sigma}^{+} c_{j\sigma} + J \sum_{<i,j>} (\mathbf{S_i} \cdot \mathbf{S_j} - \frac{1}{4} n_i n_j) \tag{1.1}$$

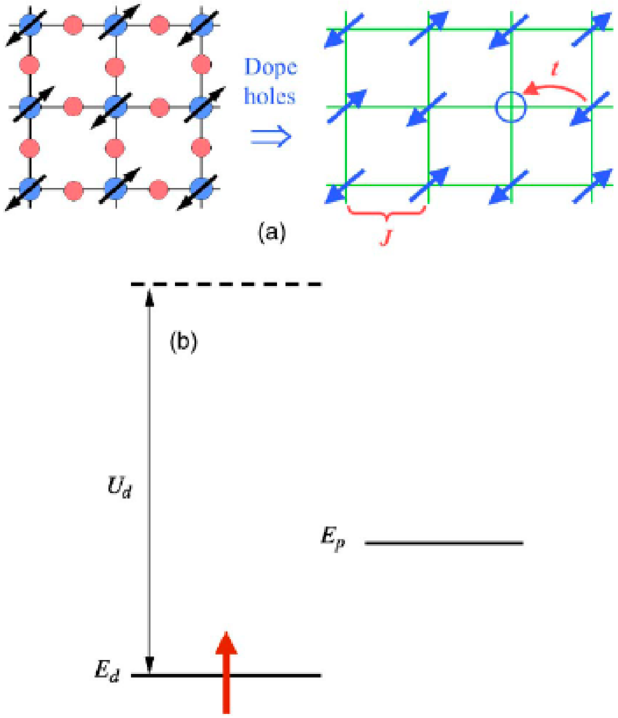

Figure 1.6: Electronic structure of cuprates. (a) Two dimensional copper-oxygen layer (left) simplified to the one band model (right). (b) The copper d and oxygen p orbitals in the hole picture. A single hole with $S = 1/2$ occupies the copper d orbital in the insulating parent compound [3].

where $n_i =$ is the number operator. The one-band $t - J$ model captures the essence of the low energy electronic excitations of the cuprates.

Phase diagram High-T_C superconductors share a common rich diagram as shown in Fig. 1.7. Take LSCO as an example. The parent compound LSCO is an antiferromagnetic insulator, with the Neel temperature $T_N \sim$ 300K. The substitution of of trivalent La by divalent Sr will add extra holes into the CuO_2 plane, and this is called doping. The AF phase is suppressed rapidly as doping increases. With further hole doping, antiferromagnetic phase is completely suppressed around 0.03∼0.05 doping and superconductivity appears with doping range 0.06∼0.30. The superconducting phase diagram forms a typical dome shape. The doping level corresponding the top of the dome or the highest T_C is called the optimal doping ∼0.16. The doping range below the optimal doping is call underdoping, the doping above is called over-doping. In the underdoping region, a pseudogap phase is found above T_C, which is not a well defined phase but a crossover. Close to the optimal doping, above T_C there is a strange metal phase where resistivity shows linear temperature dependence. This can be described by marginal Fermi liquid [18]. In the over-doping region, the normal state behaves more normally in the sense that the T dependence of resistivity is T^2 Fermi-like curve. The high-T_C cuprates can be viewed as doped Mott insulators. How the electronic structure evolves from Mott insulator to superconductor is not clear, and is the focus of this thesis.

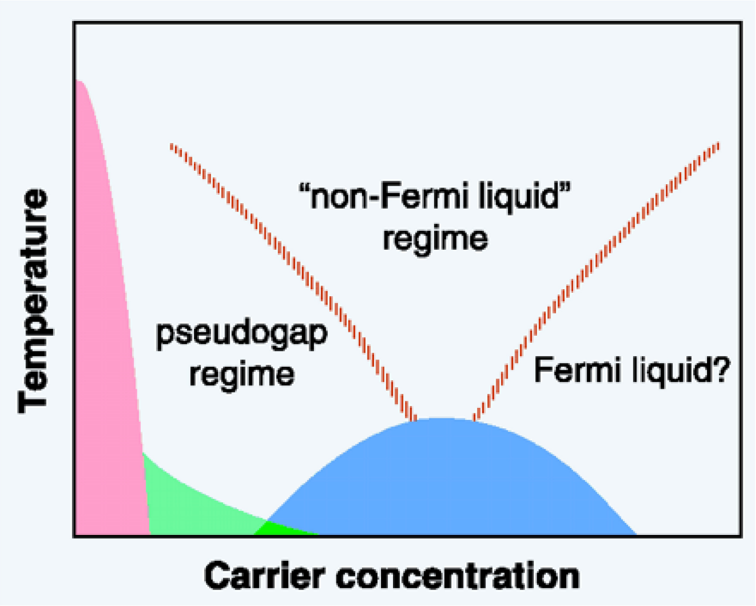

Figure 1.7: Schematic phase diagram of High T$_C$

Band structure Low energy electronic structure of the high-T_C cuprates can be described effectively by one band model. Band structures from LDA is shown in Figure 1.8 for parent compound La_2CuO_4. Cu $3d_{x^2-y^2}$ and O $2p$ form bonding and antibonding bands. The antibonding band is at the Fermi level and half filled, which should be a metal according band theory. However, the insulating nature of the parent compound indicates that simple band theory can not handle strong correlation well. The band structure can be measured directly by ARPES as shown in Fig. 1.8, which is a tight binding fit to ARPES data. The low energy band structure can be viewed as a single band structure when excluding bi-layer splitting and superlattice, which appear in some cuprate materials. Comparing LDA calculation to ARPES data, one can see the real band is highly renormalized and the band width is much narrower than the one predicted in LDA calculation. This is due to the effect of strong electron correlations. The band dispersion can be followed clearly at E_F, but at high binding energy the band structure is not clearly observed due to broad lineshape. Recently there is a high binding energy band anomaly observed around $\sim$ 350 meV. This new observation stimulate intensive debates and will be discussed later in this thesis.

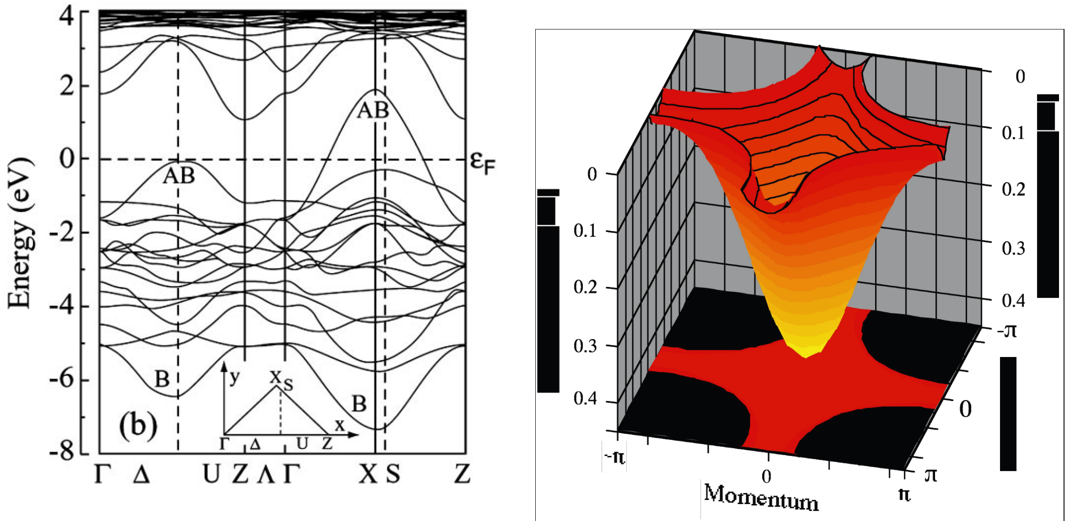

Figure 1.8: Band structure of a high-T_C cuprate superconductor. (a) LDA calculatiion of $La_{2-x}Sr_xCuO_4$. (b) The tight binding fit of the band structure of from ARPES data on $Bi_2Sr_2CaCu_2O_{8+\delta}$.

d-wave gap symmetry The symmetry of the superconducting order parameter is important to understand superconductivity. For conventional superconductors, the order parameter is isotropic s-wave. For high-T_C cuprates, the order parameter has a $d_{x^2-y^2}$ symmetry. Even though ARPES can not measure the phase of the order

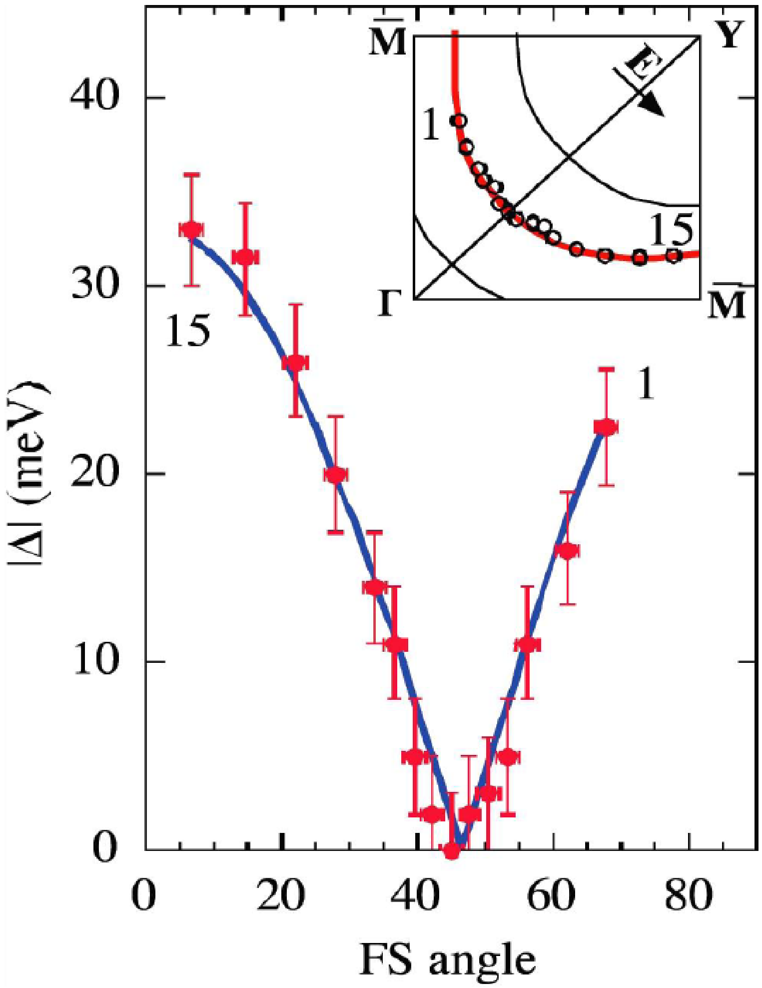

Figure 1.9: Superconducting gap in meV versus Fermi surface angle with fits to a d-wave gap(soid curve). Inset shows the locations in the zone as well as the photon polarization direction [19].

parameter, it can measure the magnitude of the gap at different k directly. Figure 1.9 shows the k-dependence of the gap along the Fermi surface [19] of optimal doped $Bi_2Sr_2CaCu_2O_{8+\delta}$. Clearly the gap is d-wave like with a node along the ΓY direction. For the over-doping region, the gap symmetry is still d-wave like,while the gap Δ_0 becomes smaller. For underdoped samples, the gap may be distorted from the pure d-wave symmetry. The nodal region gap become smaller as sample becomes further underdoped, however the antinodal gap becomes larger. Thus a two gap scenerio [6] is possible, which is the focus of this thesis.

Pseudogap One of the most unconventional phenomenon is the existence of pseudogap in the underdoped region. In the optimal doped and overdoped region, the superconducting gap closes as T goes above T_C. However, in the underdoped region, the antinodal spectra lose the coherent peak but the gap persists above T_C, known as pseudogap. The lineshape is broad and incoherent. As T goes higher, pseudogap will be filled in at some temperature, T^*, as shown in Figure 1.10. The onset of superconductivity is marked by the appearance of a sharp coherence peak near the antinode. Pseudogap becomes larger with more underdoping. The origin of pseudogap and how it is related to superconductivity are still not clear. Two scenarios are proposed: (1) one-gap scenario, pseudogap is a precursor pairing gap without phase coherence; (2) two-gap scenario, pseudogap is not related to the pairing gap and is a competing phase. Whether pseudogap phase is precursor or competing phase to superconductivity is still under debate.

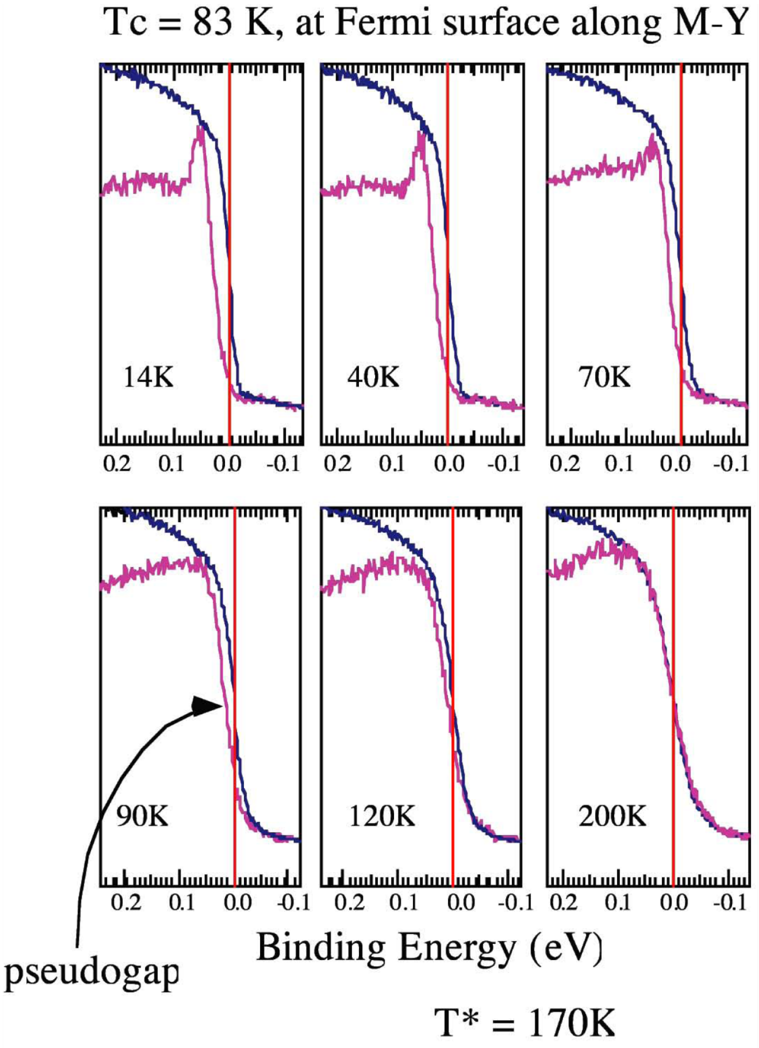

Figure 1.10: Pseudogap with $T^* = 170$ K. The spectra are at the k_F along M-Y direction, the blue lines are E_F reference from Pt spectra.

Kink A band dispersion anomaly or kink [20] was observed in 2001. The increase of momentum resolution with Scienta analyzer development made this observation possible. The kink was first observed in Bi2212, then it is observed in almost all the hole-doped curpate material and quite an universal phenomenon. The energy is about 40-70 meVs. Self energy extracted from the dispersion shows a peak shows in its real part of self energy while a drop is seen in its imaginary part. The explanation is due to a coupling to a bosonic mode, which can be a magnetic excitation or phonons.

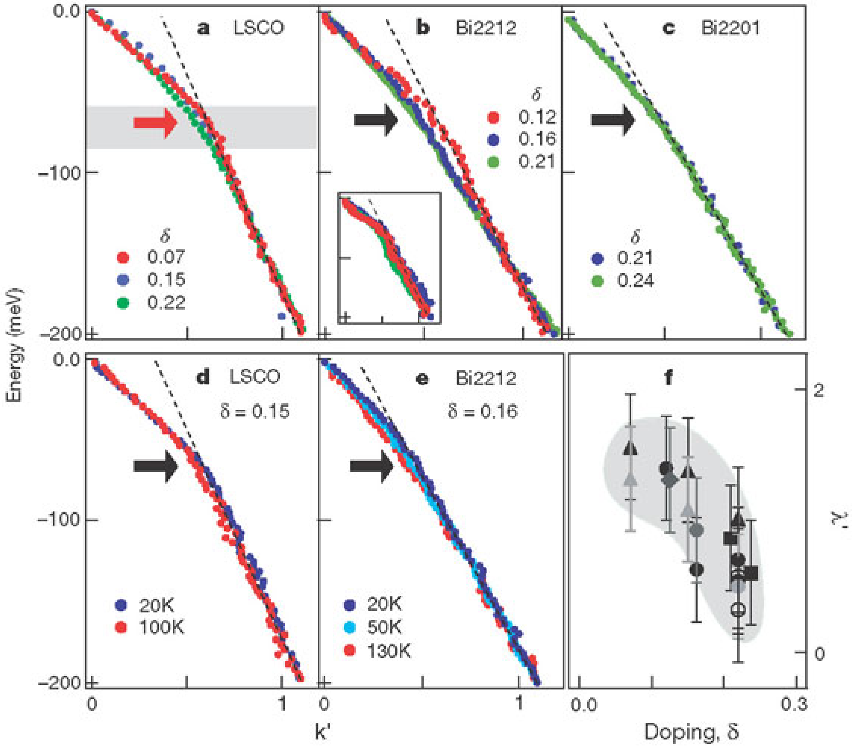

Figure 1.11: Kinks observed in LSCO and Bi2212

1.3 $\mathbf{Bi_2Sr_2Ca_{n-1}Cu_nO_{2n+4}}$

$Bi_2Sr_2Ca_{n-1}Cu_nO_{2n+4}$ has been studied expensively by ARPES due to the availability of high quality crystal and the good cleavage surface, which is crucial to ARPES. Many phenomena have been revealed by the experiments on Bi2212, such as the d-wave-like anisotropic gap [18], the pseudogap [1,10], the peak-dip-hump structure [4], the bilayer splitting [13,14]and the kink [20] etc. $Ln_xBi_2Sr_{2-x}CuO_{6+\delta}$ is single layer system with the highest $T_C = 36$K. The CuO_2 plane is separated by SrO and BiO plane, Sr can substituted by the lanthanide (La, Nd, Sm, Eu, Gd and Bi). Those substitution happens at the SrO plane, which is just above the CuO_2 plane, so the substitution can have strong effects on the electronic structure. Samples substituted by different elements exhibit different properties, so the substitution can serve as a probe to study superconductivity. The chemical substitution can have two kinds effects, changing the carrier concentration and introducing the out-of-plane disorder, but how those effects happen is still not clear. There are some advantages in studying single layer sample.

- Single CuO_2 will remove the complexity of bilayer splitting.
- Single layer sample have lower T_C, so it is easier to probe their normal state at low temperature with less thermal effect.
- $Ln_xBi_2Sr_{2-x}CuO_{6+\delta}$ can be substituted with different elements.
- $Ln_xBi_2Sr_{2-x}CuO_{6+\delta}$ can be doped continuously over wide range, from under-

doped insulator to heavily OD.

The BiO plane has a certain modulation, or superlattice, which complicates the band structure, especially at the antinodal region. The BiO planes are bounded by the Van De Valse force, which is very weak and usually the sample cleaves at BiO plane. It is much easier to get a good cleaving in BSCCO sample. Extra oxygens are believed to reside between SrO and BiO planes [16].

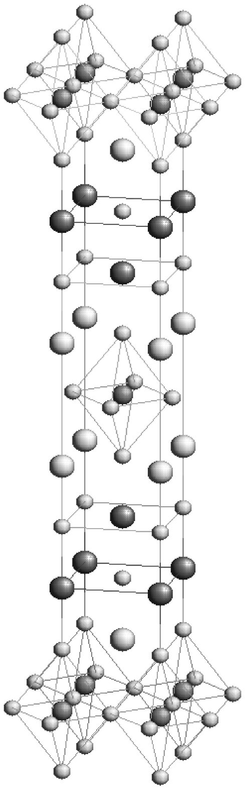

Figure 1.12: Crystal structure of $Ln_xBi_2Sr_{2-x}CuO_{6+\delta}$

Bibliography

[1] Onnes, H. K., Commun. Phys. Lab. **12**, 120 (1911).

[2] W. Meissner and R. Ochsenfeld, Naturwissenschaften **21** 787 (1933).

[3] J. G. Bednorz and K. A. Müller, Z. Phys. B. - Condensed Matter **64**, 189 (1986).

[4] M.K. Wu, Phys. Rev. Lett. **58**, 908 (1987).

[5] P. Dai, *et al*, Physica C **243**(3-4), 201 (1995).

[6] P. W. Anderson, Science **235**, 1196 (1987).

[7] P. C. Canfield and S. L. Bud'ko Scientific American **80**, April (2005).

[8] J. Bardeen*et al.*, Phys. Rev. **108**, 1175 (1957).

[9] Z. -X. Shen *et al.*, Phys. Rev. Lett. **70** 155, (1993).

[10] H. Ding *et al.*, Nature **382**, 51, (1996).

[11] A. G. Loeser *et al.*, Science **273**, 325 (1996).

[12] M. R. Norman *et al.*, Phys. Rev. Lett. **79**, 3506 (1997).

[13] D.-L. Feng *et al.*, Phys. Rev. Lett. **86**, 5550 (2001).

[14] Y. -D. Chuang *et al.*, Phys. Rev. Lett. **87**, 117002 (2001).

[15] . P. Bogdanov *et al.*, Phys. Rev. Lett. **89**, 167002 (2002).

[16] P. Richard *et al.*, Phys. Rev. B **74** 094512 (2006).

[17] F. C. Zhang *et al.*, Phys. Rev. B **37**, 3759 (1988).

[18] C. M. Varma *et al.*, Phys. Rev. Lett. **63**, 1996 (1989).

[19] H. Ding *et al.*, Phys. Rev. B **54**, R9678 (1996).

[20] P. V. Bogdanov *et al.*, Phys. Rev. Lett. **85**, 2581 (2001).

Chapter 2

Angle resolved photoemission spectroscopy

2.1 Photoemission spectroscopy

When light impinges on solids, an electron in solids can absorb a photon and be excited into an unoccupied state. If photon energy is high enough, electrons will get out of the surface and go into vacuum. This photoelectric phenomenon was first discovered by Hertz in 1887 [1], which was explained later by A. Einstein in 1905 [2] with quantization of light. Experimentally photoelectrons are analyzed with respect to their kinetic energy E and their momentum **p**. Given the energy of light and work function, the binding energy of electrons before excitation can be determined by:

$$|E_B| = h\nu - \phi - E_{kin} \tag{2.1}$$

where $h\nu$ is the incident photon energy, ϕ is the work function of the solid and E_{kin} is the kinetic energy of photoelectrons. As shown in Figure 2.1, in the case of metal,

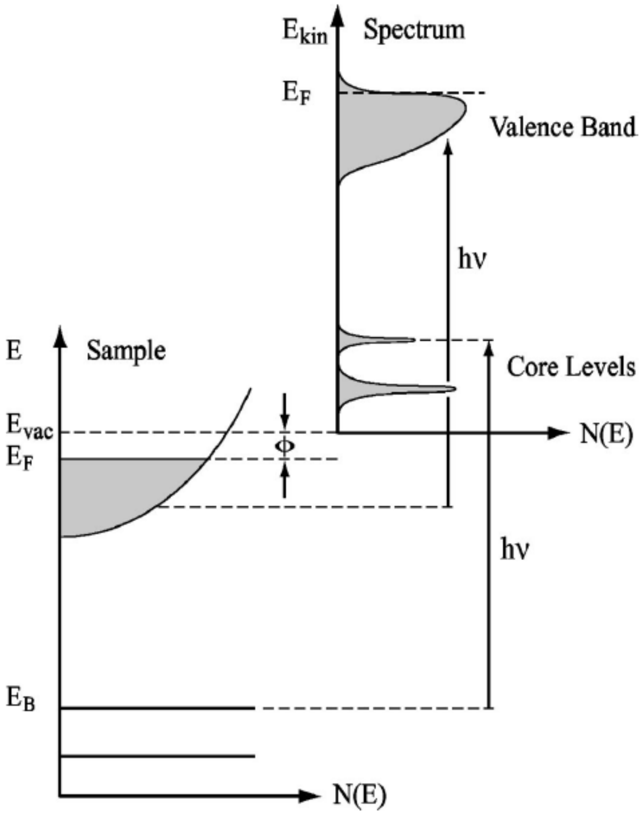

Figure 2.1: Photoemission spectroscopy [3]. Electrons with binding energy E_B absorbs an photon $\hbar\nu$ and escapes into vacuum becoming an photoelectron with kinetic energy $E_{kin} = \hbar\nu - \phi - E_B$.

core levels are at high binding energies and non-dispersing, valence bands are at low binding energies and the Fermi energy E_F is at the top of valence band and separated from vacuum by the work function ϕ. If an electron with a binding energy

E_B absorbs an photon with energy $\hbar\nu$, the electron can excited into vacuum and an photoelectron can be detected with a kinetic energy $E_{kin} = \hbar\nu - \phi - E_B$. The kinetic energy distribution of photoelectrons reflects the binding energy distribution of the electrons in solids, and can reveal detailed information about the electronic structure of solids. Based on photoelectric effect, photoemission spectroscopy(PES) was developed and has been widely used in studying the electronic structure of solids.

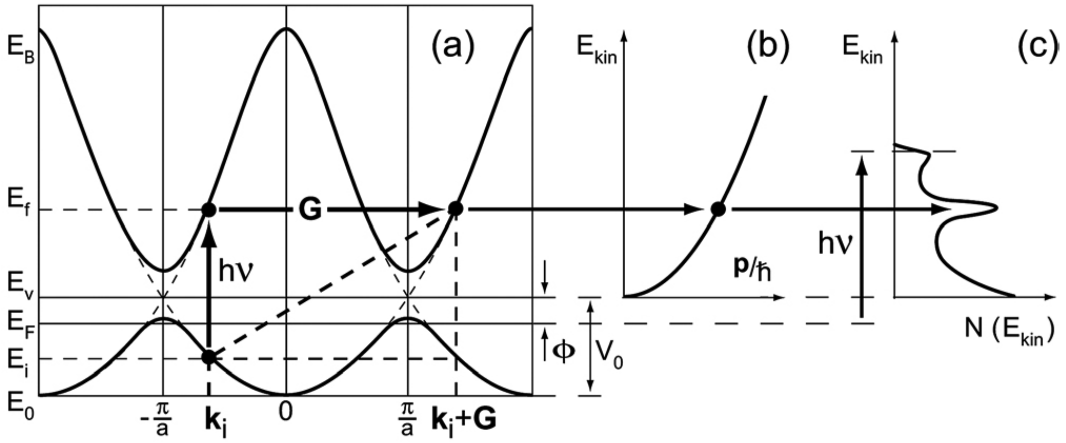

Figure 2.2: Kinematic of the photoemission process within the three-step nearly-free-electron final state model: (a) direct optical transition in the solid (the lattice supplies the required momentum); (b) free-electron final state in vacuum; (c) corresponding photoelectron spectrum, with a background due to the scattered electrons ($E_B = 0$ at E_F) [?].

The photoemission process is a single coherent process and can be rigorous and more accurately described by the one-step model [4]. The Hamiltonian includes all the processes such as buck and surface etc. However the one-step model is very complex that usually the three-step model [3] is used to describe the photoemission, in which photoemission process is divided into three independent steps:

1. Photoexcitation of an electron in solid.
2. Propagation of the excited electron to the surface.
3. Escape of the photoelectron into vacuum.

Three step model is phenomenological but has been proven to be quite successful [5–7].

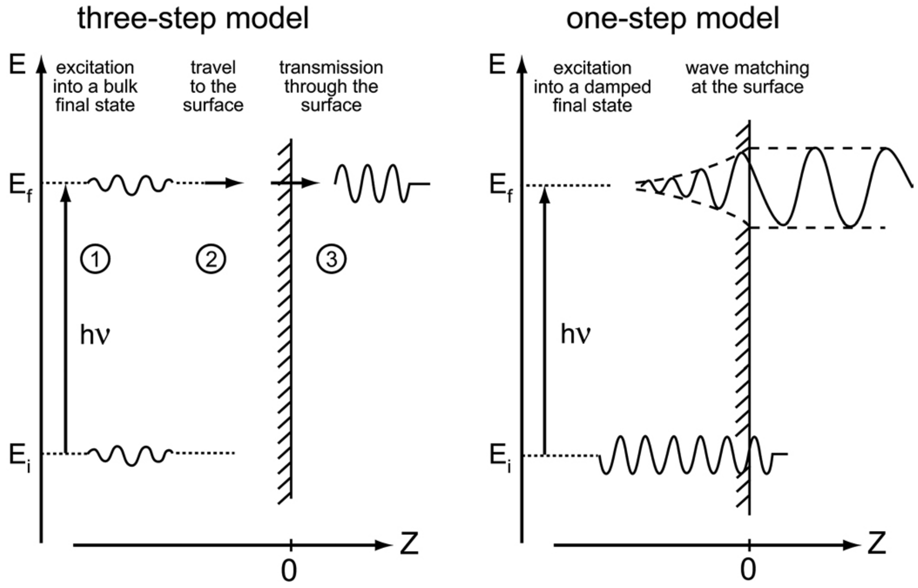

Figure 2.3: Three step model (left) and one step model (right) to describe the photoemission process.

Step one is the photon excitation process, during which an electron absorbs one photon and enters an unoccupied state. This can be described by the Fermi's golden rule:

$$w_{fi} = \frac{2\pi}{\hbar}|\langle\Psi_f^N|H_{int}|\Psi_i^N\rangle|^2\delta(E_f^N - E_i^N - h\nu) \tag{2.2}$$

where w_{fi} is the transition probability from the N-electron initial state Ψ_i^N to N-electron final state Ψ_f^N, and the interaction H_{int} is described with the dipole approximation:

$$H_{int} = -\frac{e}{mc}\mathbf{A}\cdot\mathbf{p} \tag{2.3}$$

where $\mathbf{A}$ is the electromagnetic vector potential with gauge Φ=0 and $\mathbf{p}$ is the electronic momentum operator.

Sudden approximation. During the process of photoexcitation, the system will relax after one electron is photoexcitated and can be very complex. The sudden approximation can be adopted to make the problem simpler, applicable to the high kinetic energy electrons. It assumes that once an electron absorbs a photon, its speed is so fast that the emitted electron hardly interact with the $(N-1)$ electrons left behind. With this sudden approximation, the final state Ψ_f^N can be written as a product of wave function of photoelectron $\phi_f^{\mathbf{k}}$ and the state of the remaining $(N-1)$ electrons Ψ_f^{N-1}:

$$\Psi_f^N = \mathcal{A}\phi_f^{\mathbf{k}}\Psi_f^{N-1} \tag{2.4}$$

where $\mathcal{A}$ is the operator that antisymmetrizes the wave function. Let us assume the initial state Ψ_i^N is a single Slater determinant, and write it as:

$$\Psi_i^N = \mathcal{A}\phi_i^{\mathbf{k}}\Psi_i^{N-1} \tag{2.5}$$

where $\phi_i^{\mathbf{k}}$ is the orbital from which the electron is excited and Ψ_i^{N-1} is the wave function of the remaining $(N-1)$ electrons. With this approximation, we can write the transition probability as:

$$\langle \Psi_f^N | H_{int} | \Psi_i^N \rangle = \langle \phi_f^{\mathbf{k}} | H_{int} | \phi_i^{\mathbf{k}} \rangle \langle \Psi_m^{N-1} | \Psi_i^{N-1} \rangle \tag{2.6}$$

$$w_{fi} = \frac{2\pi}{\hbar} |\langle \phi_f^{\mathbf{k}} | H_{int} | \phi_i^{\mathbf{k}} \rangle|^2 |\langle \Psi_m^{N-1} | \Psi_i^{N-1} \rangle|^2 \delta(E_f^N - E_i^N - hv) \tag{2.7}$$

where $\langle \phi_f^{\mathbf{k}} | H_{int} | \phi_i^{\mathbf{k}} \rangle = M_{f,i}^{\mathbf{k}}$ is the one electron dipole matrix element, and the second term is the (N-1) electron overlap intergral. After excitation of the electron from orbital $\mathbf{k}$, the remaining $(N-1)$ electrons are at excited states and will relax to minimize their energy. Assuming that the final state with $(N-1)$ electrons has m excited states with the wave function Ψ_m^{N-1} and energy E_m^{N-1}, the total photoemission intensity measured as a function of E_{kin} at a momentum $\mathbf{k}$ is proportional to

$$\sum_{f,i} |M_{f,i}^{\mathbf{k}}|^2 \sum_m |c_{m,i}|^2 \delta(E_{kin} + E_m^{N-1} - E_i^N - h\omega) \tag{2.8}$$

where $c_{m,i} = \langle \Psi_m^{N-1} | \Psi_i^{N-1} \rangle$ such that $|c_{m,i}|^2$ is the probability that after removal an electron from orbital $\phi_i^{\mathbf{k}}$ from N electron state and the remaining $(N-1)$ electrons will be in excited state m.

Step two is the propagation of the excited electron to the surface of solids. During the process, photoelectron can be scattered by electrons and phonons. This can be described in terms of mean free path which is inverse proportional to the probability of scattering. In most cases electron-electron interaction affects the mean free path mostly. Even though the property of materials can be very different, an universal mean free path curve can be drawn for energies of interest here, because that the electrons in solids can be approximated as free electrons. Figure 2.4 shows the general

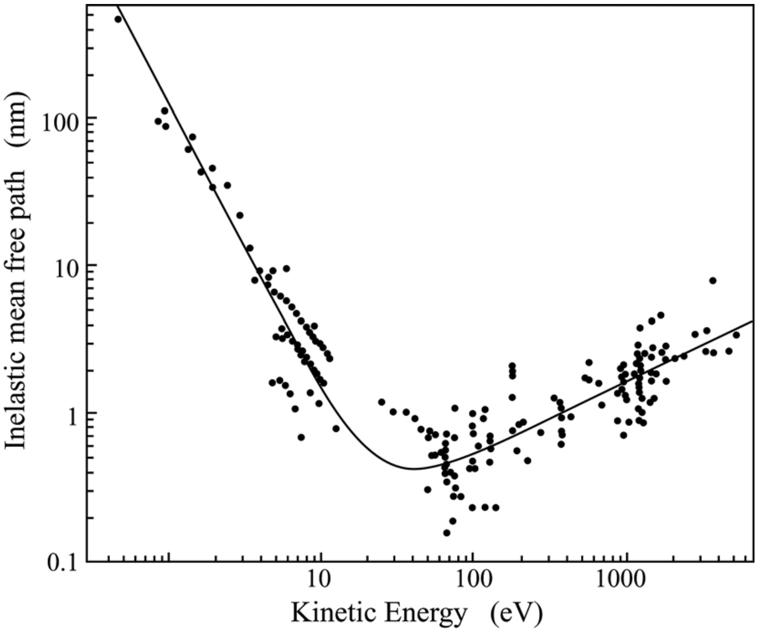

Figure 2.4: Mean free path as a function of photon energy [9]. The data is measured on many different materials.

curve of the mean free path at different energy, characterized a minimum about a few angstroms at 20 $\sim$ 100eV, which is the typical energy range widely used in ARPES. This makes ARPES a surface technique, probing the electronic states within a few layers of the surface. Therefore ARPES experiments have to be performed on atomically clean and well ordered system, implying that fresh and flat surfaces have to be prepared immediately prior to the experiment in the ultra-high vacuum (UHV) condition. Sticking coefficient S is defined as the ratio of the number of molecules that stick to a surface to the number of total molecules impinge on the surface. Assuming $S = 1$, it takes 2.5 Langmuirs (1L = 10^{-6} torr·s) to cover one layer of a surface. Now the vacuum can be as good as 2×10^{-11} torr, so it takes 13 hours to cover a surface. The sticking coefficient can be very different, depending the materials and the molecules. BSCCO cuprates can survive in a vacuum chamber for several days without observable change of spectra. To probe the bulk electronic structure of solids, one way is to increase the photon energy, called x-ray photoemission(XPS), which has poor energy and angular resolution. An alternative way is to use low photon energy, which achives very high energy and momentum resolution, but covers less BZ. The photon energy can be achieved with laser is as low as 6 eV [11].

Step three escape of photoelectrons into the vacuum. There is a potential barrier between the solid surface and the vacuum. The potential is usually called the work function ϕ, which is the minimum energy needed for an electron at Fermi energy to escape into vacuum. Only those whose kinetic energy is higher than the work function can escape into vacuum. The work function (a few eVs) can be very different from material to material.

2.2 Angle resolved photoemission spectroscopy

Figure 2.5 shows schematicaly an ARPES setup, including a light source, a sample, and a detector. When photons impinge on the surface of a sample, electrons in solid can absorb photons and escape into vaccum, which are called photoelectrons and will be collected by the detector with energy and angle resolution. The kinetic energy

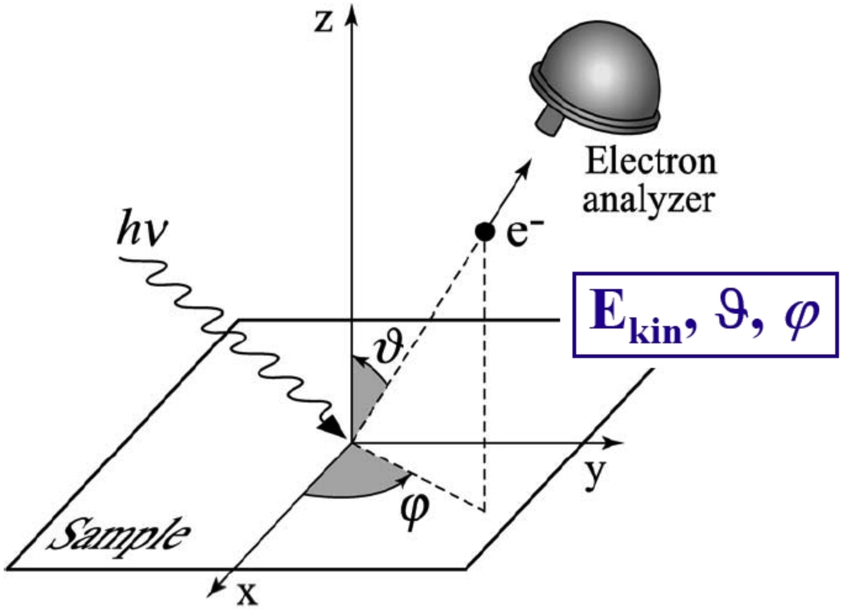

Figure 2.5: Schematic ARPES experiment [8]. Photon with energy $\hbar\nu$ impinges on the surface of samples. Electrons can absorb photon and will be excited into vacuum. Those photoelectrons will be analyzed with respect to energy and momentum by an electron analyzer.

E_{kin} can be measured and the momentum of photoelectrons can be derived easily by $p = \sqrt{E_{kin}/2m}$. During the process of photoemission, the energy E and parallel momentum $k_{//}$ are conserved and can be epxressed as below in terms of the kinetic energy E_{kin} and angle θ, ϕ:

$$k_x = \frac{1}{\hbar}\sqrt{2mE_{kin}}sin\theta cos\phi \tag{2.9}$$

$$k_y = \frac{1}{\hbar}\sqrt{2mE_{kin}}sin\theta sin\phi \tag{2.10}$$

ARPES measures the electron distribution $I(E_{kin}, \theta, \phi)$ with respect to E_{kin}, θ and ϕ, there is one-to-one mapping to $I(\omega, k_x, k_y)$. The intensity map $I(\mathbf{k}, \omega)$ can be described as:

$$I(\mathbf{k}, \omega) = A(\mathbf{k}, \omega)f(\omega)I_0(\mathbf{k}, \omega, \mathbf{A}) \tag{2.11}$$

where $A(\mathbf{k}, \omega)$ is the single particle spectral function, $f(\omega)$ the Fermi-Dirac distribution function and $I_0(\mathbf{k}, \omega, \mathbf{A})$ the magnitude of matrix element $|M_{f,i}(\mathbf{k})|^2$.

To describe an interacting many body system, Green function is introduced. Green function can be written in time-ordered $G(t - t')$, which can interpreted as the probability amplitude that one electron added to the sytem at time t will stay in the same state t'. Green function can be written in energy-momentem representation $G(\mathbf{k}, \omega) = G^+(\mathbf{k}, \omega) + G^-(\mathbf{k}, \omega)$.

$$G^{\pm}(\mathbf{k}, \omega) = \sum_m \frac{|\langle \Psi_m^{N\pm1}|c_{\mathbf{k}}^{\pm}|\Psi_i^N\rangle|^2}{\omega - E_m^{N\pm1} + E_i^N \pm i\eta} \tag{2.12}$$

where $c_{\mathbf{k}}^+$ or $c_{\mathbf{k}}^-$ creates or annihilates an electron with energy ω, momentum $\mathbf{k}$ in the initial state Ψ_i^N, and η is a positive infinitesimal. The one particle spectral function $A(\mathbf{k}, \omega) = -(1/\pi)ImG(\mathbf{k}, \omega)$ as:

$$A^{\pm}(\mathbf{k}, \omega) = \sum_m |\langle \Psi_m^{N\pm1}|c_{\mathbf{k}}^{\pm}|\Psi_i^N|^2 \delta(\omega - E_m^{N\pm1} + E_i^N) \tag{2.13}$$

Green function can expressed in terms of self energy $\Sigma(\mathbf{k}, \omega) = \Sigma'(\mathbf{k}, \omega) + \Sigma''(\mathbf{k}, \omega)$, which include the information of interaction. Green function can be written as:

$$G(\mathbf{k}, \omega) = \frac{1}{\omega - \epsilon_k - \Sigma(\mathbf{k}, \omega)} \tag{2.14}$$

$$A(\mathbf{k},\omega) = -\frac{1}{\pi}\frac{\Sigma''(\mathbf{k},\omega)}{[\omega-\epsilon_{\mathbf{k}}-\Sigma'(\mathbf{k},\omega)]^2+[\Sigma''(\mathbf{k},\omega)]^2} \tag{2.15}$$

There are some sum rules about the spectra function:

$$\int_{-\infty}^{\infty} d\omega A(\mathbf{k},\omega) = 1 \tag{2.16}$$

$$\int_{-\infty}^{\infty} d\omega f(\omega)A(\mathbf{k},\omega) = n(\omega) \tag{2.17}$$

Given the spectral function $A(\mathbf{k},\omega)$, band dispersion and self energy can be extracted. At fixed $\mathbf{k}$, the position where has maximum intensity gives $\omega-\epsilon_{\mathbf{k}}-\Sigma'(\mathbf{k},\omega) = 0$. This corresponds to $\omega = \epsilon_{\mathbf{k}} + \Sigma'(\mathbf{k},\omega)$, which is the renormlized band disperion. For interacting systems, self energy Σ includes all the information about interactions, which make ARPES a powerful technique in probing the properties of solids. Assuming the self energy Σ is $\mathbf{k}$ independent, then Σ can be extracted from ARPES data. With bare band $\epsilon_{\mathbf{k}}$ approximated by LDA calculation or just a linear approximation $\epsilon_{\mathbf{k}} = \mathbf{v_F}\cdot(\mathbf{k}-\mathbf{k_F})$, we can get:

$$\Sigma'(\mathbf{k},\omega) = \omega - \epsilon_{\mathbf{k}} \tag{2.18}$$

Approximately, $A(\mathbf{k},\omega)$ has a lorentzian lineshape with maximum of $-\frac{1}{\pi}\frac{1}{\Sigma''(\mathbf{k},\omega)}$, so that the width of half maximum can be reached that:

$$-\frac{1}{\pi}\frac{\Sigma''(\mathbf{k},\omega)}{[\omega-\epsilon_{\mathbf{k}}-\Sigma'(\mathbf{k},\omega)]^2+[\Sigma''(\mathbf{k},\omega)]^2} = -\frac{1}{2\pi}\frac{1}{\Sigma''(\mathbf{k},\omega)} \tag{2.19}$$

Solving this equation will give:

$$\Sigma''(\mathbf{k},\omega) = \frac{1}{2}(\epsilon_{k2}-\epsilon_{k1}) = \frac{1}{2}\frac{\partial\epsilon_{\mathbf{k}}}{\partial\mathbf{k}}\Delta\mathbf{k} \tag{2.20}$$

By measuring the width of the constant energy line, we can extract the imaginary part of self energy. In fact the real part and imaginary part of the self energy are related by Kramers-Kronig relation, meaning with one of them we can derive the other. We can measure both of them from ARPES data. This analysis have been done many times and demonstrated its power in probing electron-phonon interactions and other electrons interaction with other collective modes.

Figure 2.6 shows a typical 2-dimensional intensity map $I(\mathbf{k}, \omega)$. The x-axis is the momentum and y-axis is the energy, the value gives the counting of photoelectrons at that momentum and energy.

There are two ways to view an ARPES spectrum. The data analyzed through a constant momentum line is called as energy distribution curve (EDC), the data analyzed through a constant energy line is called as momentum distribution curve (MDC) [8]. Those two curves are used frequently in the analysis of ARPES data. EDC function can be expressed as below:

$$I_{EDC}(\omega) = I_0(\mathbf{k}_{const}, \hbar\nu, \mathbf{A}) \frac{1}{\pi} \frac{\Sigma''(\mathbf{k}, \omega)}{[\omega - \epsilon_{\mathbf{k}} - \Sigma'(\mathbf{k}, \omega)]^2 + [\Sigma''(\mathbf{k}, \omega)]^2} f(\omega) \qquad (2.21)$$

We can see that EDC spectra involves the almost constant matrix element, this is an advantage of the EDC analysis. However, an EDC has a non-trivial ω-dependence: (i) an EDC is not a lorentzian or any simple function; (ii) an EDC has the Fermi function term, which makes it asymmetric; (iii)its peak postion is not given by the pole condition; (iv) at last the EDC width, is not only depend on the imaginary part of the self energy Σ'', but also the real part of the self energy Σ'. All of those make the

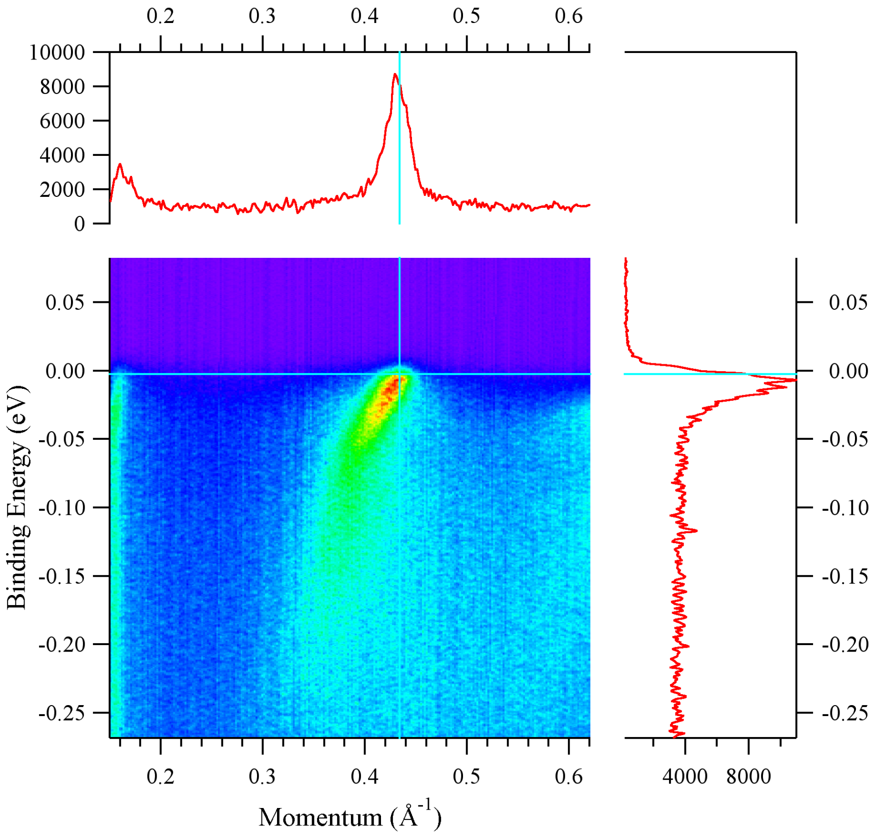

Figure 2.6: ARPES intensity map. The image plot is a typical ARPES intensity map. The upper panel is the MDC line. The right one is the EDC line.

data analysis on an EDC complicated. After the development of the Scienta analyzer, which can measure the two-dimensional map at the same time with better resolution, MDC analysis becomes available.

$$I_{MDC}(\mathbf{k}) = I_0(\mathbf{k}, h\nu, \mathbf{A}\frac{1}{\pi}\frac{\Sigma''(\mathbf{k},\omega)}{[\omega - \epsilon_{\mathbf{k}} - \Sigma'(\mathbf{k},\omega)]^2 + [\Sigma''(\mathbf{k},\omega)]^2} f(\omega_0) \tag{2.22}$$

MDC analysis has some advantages: (i) in the vincity of the Fermi energy, the MDC lineshape is symmetric lorentzian; (ii) MDC will not be affected by the Fermi function.

2.2.1 Matrix element

The measured intensity of is the product of the spectral function $A(\mathbf{k}, \omega)$, the Fermi function $f(\omega)$and the matrix element $I_0(\mathbf{k}, \omega, \mathbf{A})$. The matrix element depends on photon energy, geometry setting and light polarization. Sometimes the matrix element can suppress the photoelectron intensity, which is not good for measuring the spectral function; on the other hand, we can also choose different matrix elements to enhance some bands while suppressing others. This can also give us some information about the electronic structure of solids. The matrix element can be written as:

$$M^{\mathbf{k}}_{f,i} = \langle \phi^{\mathbf{k}}_f | -\frac{e}{mc}\mathbf{A} \centerdot \mathbf{p} | \phi^{\mathbf{k}}_i \rangle \tag{2.23}$$

By using the commutation relation $\hbar\mathbf{p} = -i[x, H]$, matrix element can written as:

$$\langle \phi^{\mathbf{k}}_f | -\frac{e}{mc}\mathbf{A} \centerdot \mathbf{p} | \phi^{\mathbf{k}}_i \rangle = \langle \phi^{\mathbf{k}}_f | -\frac{e}{mc}\mathbf{A} \centerdot \mathbf{r} | \phi^{\mathbf{k}}_i \rangle \tag{2.24}$$

ARPES usually is done in the UHV region, ranging a few eV to a few hundred eV. For $\hbar\omega = 10$ eV, one has $\lambda = 10^3$ Å, which is much larger than the lattice constant and therefore A can be taken as constant. As shown in Figure 2.7a, the initial orbital

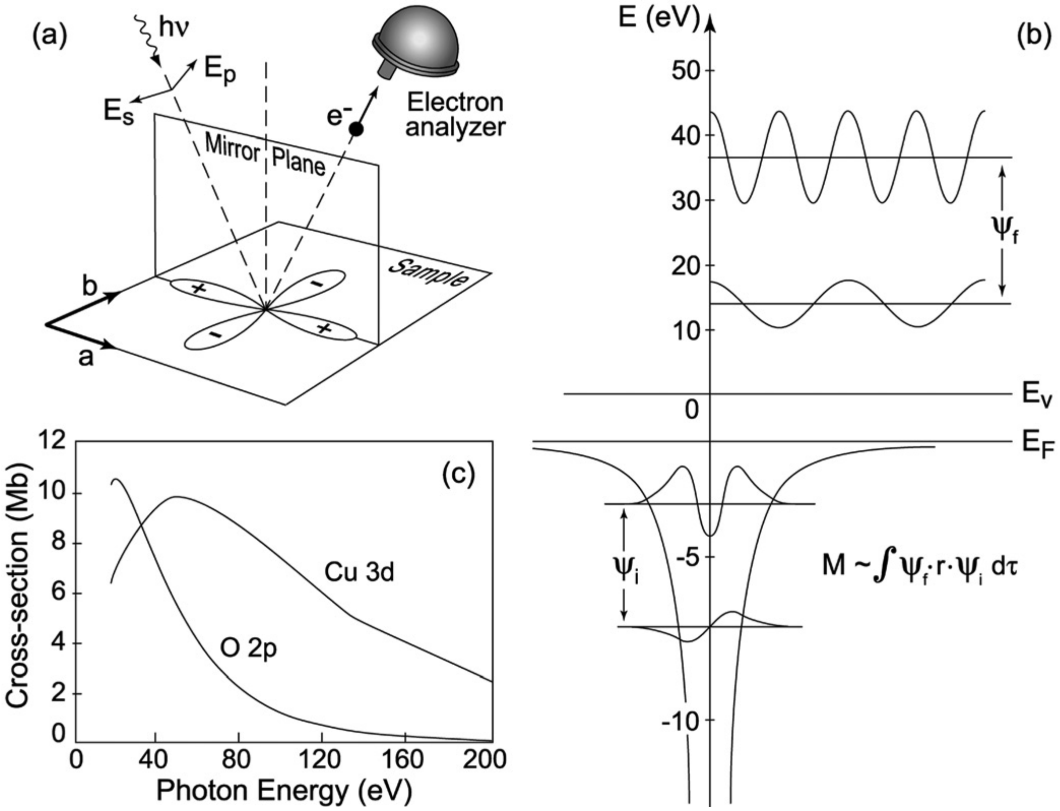

Figure 2.7: (a) Mirror plane emission from a $d_{x^2-y^2}$ orbital. (b) Sketch of the optical transition between atomic orbitals with different angular momenta (the harmonic oscillator wavefunctions are here used for simplicity) and free electron wavefunctions with different kinetic energies [3]. (c) Calculated photon energy dependence of the photoionization cross-sections for Cu 3d and O 2p atomic levels [13].

has the $d_{x^2-y^2}$ symmetry, which is even with respect to the mirror plane. The final state is taken as plane waves $e^{i\mathbf{k}\cdot\mathbf{r}}$, for those k whose direction is even to the mirror plane the intensity is strong; for those k whose direction is odd to the mirror plane, the total integral will be zero. To get a finite photoemission intensity, the final state should follow:

$$\langle\phi_f^{\mathbf{k}}| - \frac{e}{mc}\mathbf{A}\cdot\mathbf{r}|\phi_i^{\mathbf{k}}\rangle \begin{cases} \phi_i^{\mathbf{k}} \quad \mathit{even} \quad \langle+|+|+\rangle \quad A \quad \mathit{even} \\ \phi_i^{\mathbf{k}} \quad \mathit{odd} \quad \langle+|+|+\rangle \quad A \quad \mathit{odd} \end{cases}$$

The matrix element also depends on photon energy. Assuming that the photoelectron is a plane wave $e^{i\mathbf{k}\cdot\mathbf{r}}$, one can rewrite the matrix element as :

$$|M_{f,i}^{\mathbf{k}}|^2 \propto |\langle\phi_f^{\mathbf{k}}|\mathbf{A}\cdot\mathbf{r}|\phi_i^{\mathbf{k}}\rangle|^2 \propto |(\mathbf{A}\cdot\mathbf{k})\langle\phi_i^{\mathbf{k}}|e^{\mathbf{k}\cdot\mathbf{r}}\rangle|^2 \tag{2.25}$$

When incident photon energy increases, the momentum $\mathbf{k}$ and the kinectic energy increase. Thus the matrix element changes. As shown in Figure 2.7c, the cross section of Cu $3d$ and O $2p$ are photon energy dependent. Besides its photon energy dependence, the matrix element $|M_{f,i}^{\mathbf{k}}|^2 \propto |\mathbf{k}\cdot\mathbf{k}|^2$ causes the intensity to zero when the system is symmetry forbidden.

2.3 Experimental instrumentation

An ARPES system composes of several subsystem, including detector, light source, and vacuum system.

Detector ARPES measures a continuous spectra of photoelectron intensity as a function of kinetic energy and space angle. This is done by an electron energy analyzer. There are many types of electron analyzers using different mechanism. Four methods can be used to analyze the energy of an electron [3]:

1. Resonances in a scattering process.

2. Time-of-flight.

3. Deceleration of an electron using a retarding electric field.

4. Change of the orbital of a particle by an electric or magnetic field.

Now most detectors used in ARPES are hemispherical detectors, which use the forth method to convert energy resolution into space resolution. The mechanism of energy analyzer is shown schematically as in Figure 2.8, consisting of an inner and an outer hemispheres, with radius R_1 and R_2. High voltage is connected to the two hemispheres separately with voltage difference ΔV. The electric field generated between the inner and outer hemspheres will allow eletrons with a narrow kinetic energy range to pass through, all other electrons will hit the inner or outer plate. The energy is pass energy $E_{pass} = e\Delta V/(R_1/R_2 - R_2/R_1)$. Electrons will be retarded or accelerated to this kinetic energy to pass through.

Electrons lens. The lens can retard the electrons to the energy that can be detected by the analyzer. Two dimensional high resolution detector is mounted at the exit slit of analyzer. The detector is highly position resolved, and can convert electrons into light, which can be detected by a CCD camera. The resolution measured with E_{pass} is determined by the radius and the slits, $\Delta E_\alpha = E_{pass}(w/R_0 + \alpha^2/4)$.

Detectors manufactured by Scienta have been used to collect data in this work. The Scienta detector can measure the 2 dimensional spectrum simutaneouly and can

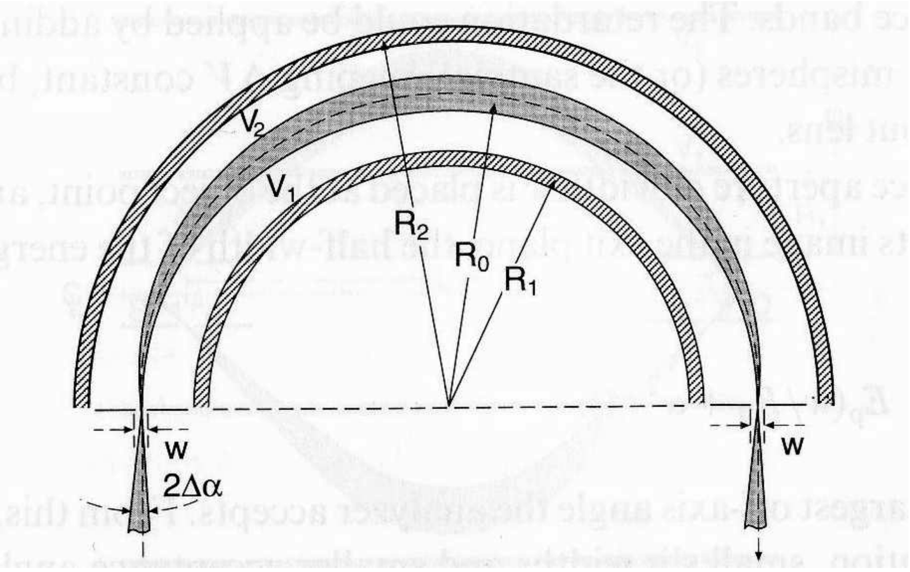

Figure 2.8: Hemispherical electron analyzer [3]. The inner and outer hemispherical plates are connected with high voltage V1 and V2 with radius R1 and R2.

achieve high energy resolution and momentum resolution. The detector consists three parts : (1) hemispherical energy analyzer; (2) electron lens; (3) two dimensional high resolution electron detector. As shown in Figure 2.9, the electron lens collect photoelectrons. With a retarded potential, the lens can retard photoelectrons and reduce its kinetic energy to E_{pass} and spread the electrons from different angles to different positions at the entrance slit. At each angle, electrons have an energy dispersion. Then at the exit slit, the photoelectron spectrum has been convert into a space resolution. A detector is mounted at the end of exit slit to detect photoelectrons, which includes a micro channel plane (MCP) and a phosphor plane in series, the light will be detected by a CCD camera. The product Seienta R4000 can achieve: (1) A submev

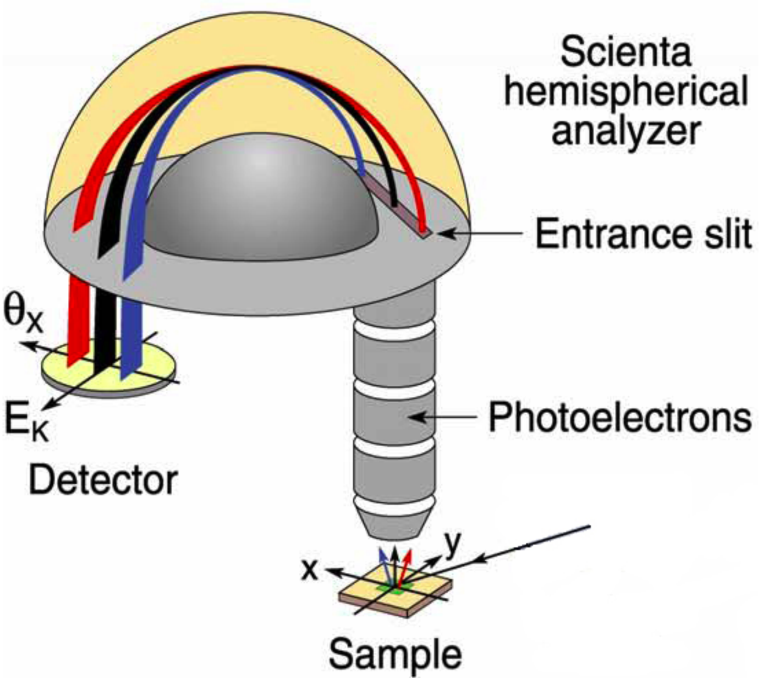

Figure 2.9: Scienta hemispherical detector. The detector is composed of a photoelectron lens, a hemispherical analyzer and a detector.

resolution; (2) a 4000 resolving power; (3) a 30 degrees wide acceptance angle; (4) can work with up to 10 keV kinetic energy.

Light source The light source used in ARPES should be able to provide high intensity monochromized photons. The work function ϕ of a typical material is about 4-5 eV, so the photon energy should be higher than this. Usually ARPES experiments are performed at the photon energy range from a few electronvolts to a few hundred electronvolts. There are three kinds of light sources used in ARPES system, synchrotron light, gas discharge lamp, and Laser. As for this work, most data was done with synchrotron light and gas discharge lamps.

Synchrotron radiation When charged particles move at at a relativistic velocity and are accelerated perpendicular to their trajectory, there will be electromagnetic radiation by particles. The acceleration is usually achieved by magnetic fields. Due to the relativistic energy of the particles the generated light has superior properties. If the electron is relativistic, the radiation emission occurs tangentially to the trajectory and the beam is highly focused. The synchrotron light is usually a continuous spectrum. Grating is used to get monochronized light. Close to the chamber, light is focused with mirrors. The diagram is shown as Figure 2.10.

Synchrotron light has several advantages:

- High brightness.
- Wide energy range, from infrared to hard X-ray.

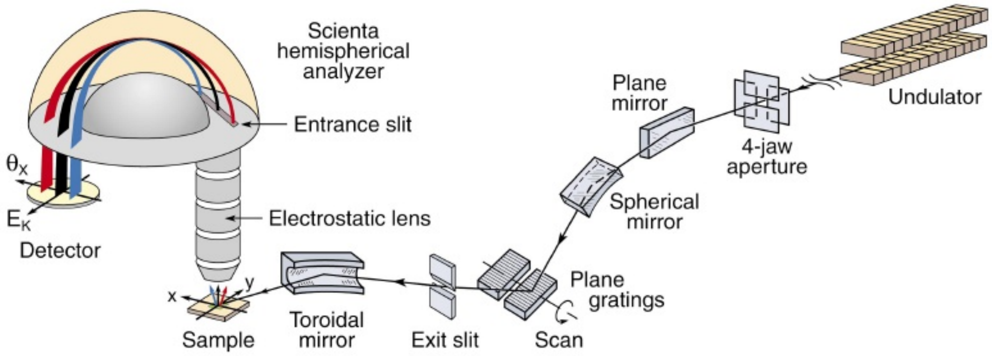

Figure 2.10: Schematic diagram of PGM Beam line.

- High polarization.

Beamline 12.0.1.1 is the ARPES branch of beamline 12 at Advanced Light Source as show in Figure 2.10. Coming out from a U8 undulator, light can be monochromized by two plane VLS gratings: one has 200 lines per mm, the other one has two different ruling densities a 300 lines per mm and 600 line per mm area. The 300 line grating is optimized for 50-75 eV , The 600 line grating is optimized for 125 eV with a maximum resolving power of 10,000. This work has been collected with synchrotron beam at Advanced Light Source (ALS) beam line BL12, Synchrotron Radiation Centers (SRC) U1-NIM and PGM, and National Synchrotron Light Source (NSLS) U13. Different beamlines have optimal performance at different energy range and different end station. The 200 line/mm grating at ALS BL12 can provide 10^{13} photons/s at 134 eV, which is quite bright. The energy range is from 20 to 320 eV.

Helium discharge lamp Helium lamp utilizes the Helium resonance lines as monochromized ultraviolet light source. Helium has two characterized lines: HeI energy is 21.2 eV and HeII energy is at 42 eV. Several characters make He lamp a good light source: (1) The energy is good energy range for ARPES experiment; (2) The line width of He resonance is 10 meV or less; (3) He gas is inertial element and has weak contamination effect to most samples after using small apertures and differential pumping between the lamp and the sample chamber. The new generation He lamp utilize the Electron Cyclotron Resonance(ECR) mechanism to produce low pressure He plasma. ECR is created in a small metallic discharge cavity by the application of a strong permanent magnetic field B, perpendicular to the microwave E vector. Under ECR, electrons will move in a circular motion with a frequency of 10 GHz microwave. The circulation motion in the cavity will increase the probability of electrons colliding with He atoms, and produce a high flux of radiation. Low pressure of of He can increase the intensity ratio of HeII to HeI. This design can produce HeI with linewidth of 1.1 meV. He lamp setup include: (1) microwave generator; (2) resonance cavity; (3) He source; (4) differential pump; (5) grating. He lamp have two lines, He I_α and I_β, a grating is introduced to get monochronized light. At the same time, the grating can work as a focusing mirror. There are some disadvantages of He lamp: (1) the flux is not as high as an undulator beamline; (2) the photon energy can not be changed; (3) the gas flow will get into the measurement chamber without a filter; (4) light spot is large so momentum resolution is not good, thus a large flat

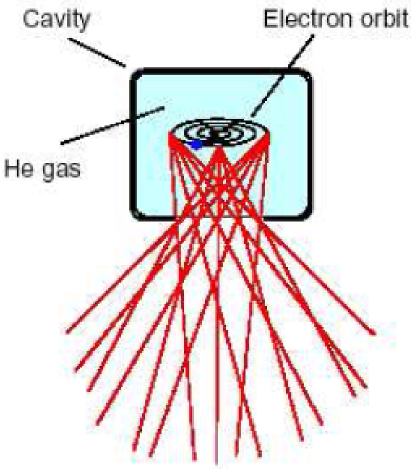

Figure 2.11: Low pressure helium gap in a small cavity is excited by ECR electrons to produce high intensity UV radiations.

surface is necessary.

Vacuum system ARPES experiment is usually performed with photon energy 10-100eV, with the mean free path about 5-20Å, just the top most layers of the sample. A fresh and flat surface of sample is critical to ARPES measurement. To do this, samples must be cleaved and measured in a UHV environment. So UHV is important to ARPES.

Bibliography

[1] H. Hertz, Ann. Physik **31** 983 (1887).

[2] A. Einstein, Ann. Physik **17** 132 (1905).

[3] Hüfner, S., "Photoelectron Spectroscopy", (Springer-Verlag, Berlin, 1995).

[4] Mahan, G. D., Phys. Rev. **B**, 4334 (1970).

[5] Feibelman, P. J., and Eastman, D. E., Phys. Rev. B **10**, 4932 (1974).

[6] Fan, H. Y., Phys. Rev. **68**, 43 (1945).

[7] Berglund, C. N., and Spicer, W. E., Phys. Rev. **136**, A1030 (1964).

[8] Damascelli, A., Hussain, Z. and Shen, Z. -X., Rev. Mod. Phys. **75**, 473 (2003).

[9] Seah, M. P. and Dench, W. A., Surf. Interface Anal. 1, 2 (1979).

[10] S. Souma, T. Sato, and T. Takahashi, Rev. of Sci. Instrument **78**, 123104 (2007).

[11] J. D. Koralek et al., Phys. Rev. Lett. **96**, 017005 (2006).

[12] T. Valla *et al.*, Science **285**, 2110 (1999).

[13] J. J. Yeh *et al.*, Atom. Data Nucl. Data Tabl. **32**, 1 (1985).

Chapter 3

Disorder and Coulomb-like Gap

3.1 Introduction

It is a common belief that the origin of the pseudogap in cuprates is critically related to the understanding of high-Tc superconductivity. Direct observation of the pseudogap, as in angle-resolved photoemission spectroscopy(ARPES) [1] and scanning tunneling microscopy(STM), are mostly done on the $\mathrm{Bi_2Sr_2Ca}_n\mathrm{Cu}_{n+1}\mathrm{O}_{2n+6}$ compounds, whose doping range is limited through oxygenation. More heavily underdoping can only be achieved by chemical substitution [10]. A recent ARPES investigation of the pseudogap in $\mathrm{Bi_{2.1}Sr_2Ca}_{1-x}\mathrm{Y}_x\mathrm{Cu_2O_8}$ [17] within this low doping regime revealed different pseudogap behaviors for the nodal and antinodal regions, interpreted in terms of two different gaps. in high-T_c cuprates.

Inhomogenuity has been observed in Bi2212 by STM, and it may be important to

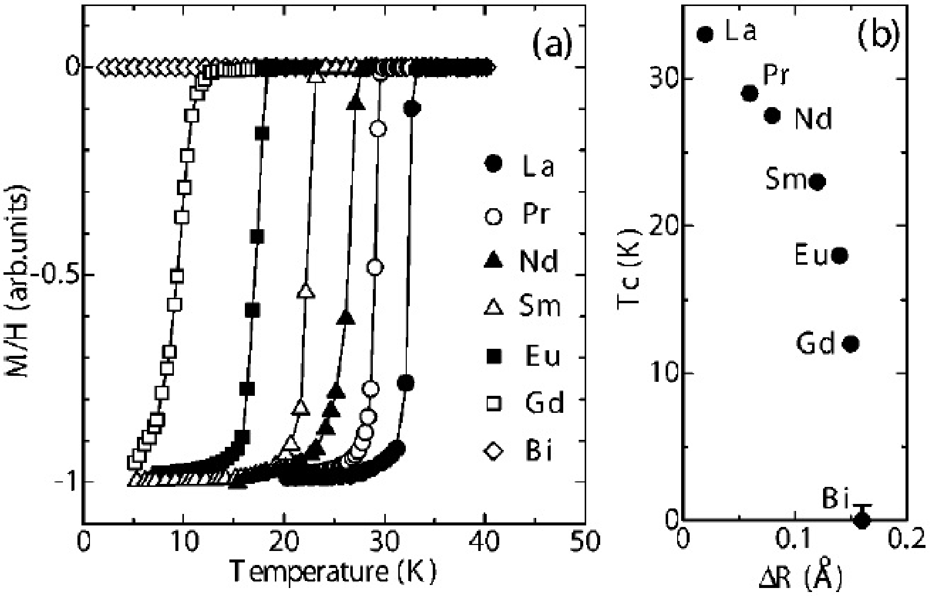

Figure 3.1: LnBi2201

high-T_c superconducting . High-T_c cuprates can be doped to have superconductivity. The doping is usually achieved by introducing more oxygen or by chemical substitution, which will inevitably introduce disorder. There are many different families of materials with different T_cs, some of these T_c differences may result from the influence of the disorder. The crystals of $Bi_2Sr_{2-x}Ln_xCuO_{6+\delta}$ were synthesized with Ln = (La, Pr, Nd, Sm, Eu, Gd, Bi) [10] as shown in Fig 3.1. The maximum T_c will decrease as the substitution element number increases. We know that the ion size will decrease as element number increases. The decrease of maximum T_c has been attributed to the mismatch of Ionic size Δr [9], which can be viewed as a measure of disorder. How superconductivity is influenced by disorder is far from clear.

To study the influence of disorder, one way is to fix the substitution content and to change the substitution element, the other way is to fix the substitution element and to change the substitution content. A serial of high quality single crystals of $Bi_2Sr_{2-x}Bi_xCuO_{6+\delta}$ were grown by the traveling solvent floating zone method [4], with x from 0.02 to 0.5, which are good candidates to study the problem of disorder. Maximum T_c is 9K at x=0.05, thus it is a very good candidate for studying the low temperature normal state properties. T_c of the superconducting samples was determined by AC susceptibility, the superconducting transition width is about 0.5-1.3K. ARPES experiment were performed at the beamline U1NIM of the Synchrotron Radiation Center in Wisconsin, and the beamline 12.01 of the Advanced Light Source in California. Energy and momentum resolutions have been set to 10 - 20 meV and 0.02 Å^{-1}, respectively. All samples were cleaved and measured in situ in a vacuum better than 8×10^{-11} Torr on a flat (001) surface.

3.2 $Bi_{2+x}Sr_{2-x}CuO_{6+\delta}$

Stoichastic Bi2201 does not exist, the reason is still not clear. So all the material of Bi2201 have some chemical substitution. Sr can be substituted by Ln(La, Gd, Bi) and Bi can be substituted by Pb. The latter is usually to remove the Bi-O modulation that makes the electronic structure more complex. The extra oxygen usually are believed to reside between the SrO and CuO2 plane. Ln-Sr substitution occurs at SrO_2 plane, which is just next to the CuO2 plane, so this substitution may have strong effect on

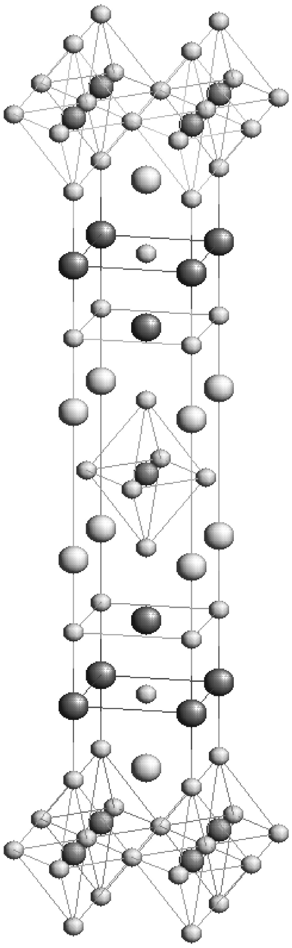

Figure 3.2: Crystal structure of $Bi_{2+x}Sr_{2-x}CuO_{6+\delta}$.

the electronic structure. As in Fig 1.12, the red dot is CuO2 plane. and the SrO is just next to CuO2 plane. BiO plane is far from CuO plane. The two BiO planes are bounded by the Van De Vaals force,which is very weak and usually the sample cleaves at between BiO plane. This make it easily to get a good flat surface, which is important to ARPES measurement.

3.3 Resistance of $\mathrm{Bi}_{2+x}\mathrm{Sr}_{2-x}\mathrm{CuO}_{6+\delta}$

Resistance of $\mathrm{Bi}_{2+x}\mathrm{Sr}_{2-x}\mathrm{CuO}_{6+\delta}$ has been measured carefully for all the samples as shown in Fig. 3.3 [4]. Low substituted samples with x=0.05, 0.1, 0.15 shows superconductivity at low temperatures. As temperature decreases, resistance of x=0.05 decreases monotonically, which is a character of overdoped sample. For samples with x=0.1 and 0.15, the upturn of resistance at low T is the characteristic feature of underdoping. No superconductivity is observed above T=1.6K on those samples with $x > 2.0$. Resistance of samples with x=0.31 or higher show a divergence as T goes down. The transition width is narrow 0.5∼1K, which means good uniform quality of samples. Post annealing under different temperature and atmosphere has been widely used to change the doping level of samples. But it is difficult to change T_C of $\mathrm{Bi}_{2+x}\mathrm{Sr}_{2-x}\mathrm{CuO}_{6+\delta}$by annealing. Samples has been annealed in oxygen or nitrogen atmosphere from 400 to 600 °C for 100 hours, but the largest change of T_c in AC susceptibility curve is less than 0.5K. Those samples are very stable.

We show in Fig. 3.4 the evolution of the Fermi surface of $\mathrm{Bi}_2\mathrm{Sr}_{2-x}\mathrm{Bi}_x\mathrm{CuO}_{6+\delta}$ at

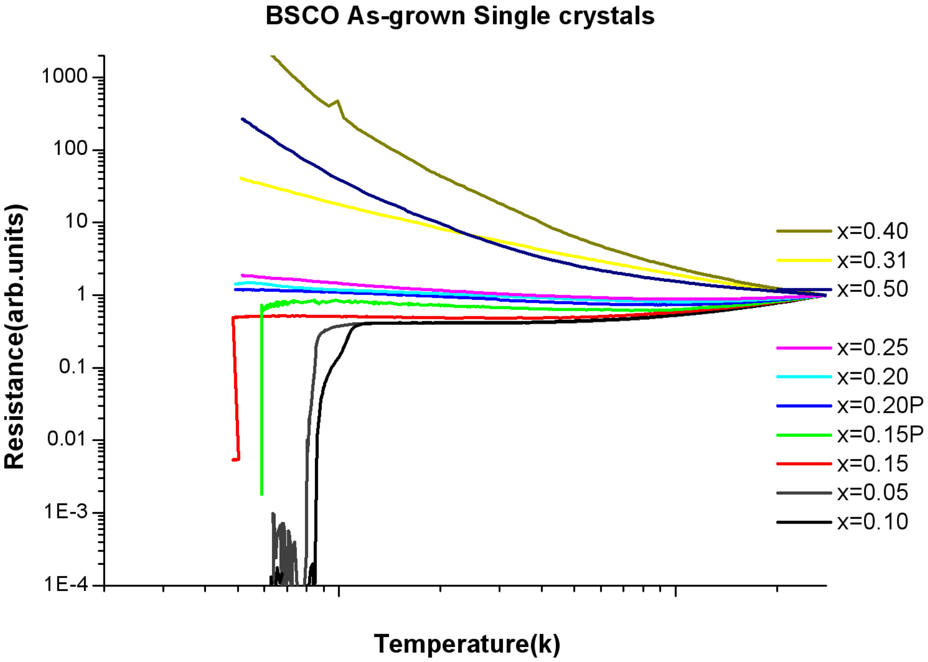

Figure 3.3: Resistance of $Bi_{2+x}Sr_{2-x}CuO_{6+\delta}$samples with different Bi content. All the data are normalized to the high temperature end.

20 K for six different Bi contents from $x = 0.05$ to 0.4. The Fermi vectors extracted from the momentum distribution curve (MDC) peaks are consistent with the intensity plots and allow a precise determination of the underlying FS, which is defined as a contour of the minimum gap locus [5]. We report in Fig. 3.4g all the underlying FS extracted for the various Bi concentrations using an effective tight-binding fit. We notice a smooth evolution in the shape of the FS. In particular, the FS at the antinodes moves away from the M(π, 0) point as the Bi content increases. More importantly, as shown more clearly in Fig. 3.4g, the size of the Y(π,π)-centered hole-like FS decreases continuously with the Bi concentration, indicating the underdoping nature of the $\mathrm{Sr}^{2+}\rightarrow\mathrm{Bi}^{3+}$ substitution.

We extract experimental values of the effective hole-doping p and plot them as a function of the Bi substitution x in Fig. 3.4h, by using Luttinger theorem, which states that the volume of an enclosed FS is proportional to the carrier concentration $1+p$. While the derived doping p decreases linearly with x, as shown in Fig. 3.4h, the linear fit gives $p = 0.182 - 0.36x$, which indicates that each substituting Bi atom removes only 0.36 hole-like carrier from the $\mathrm{CuO_2}$ plane. A similar result, albeit with an even smaller doping efficiency, has been observed in $\mathrm{Bi_2Sr_{2-x}La_xCuO_{6+\delta}}$ (La-Bi2201) by Hall measurements [6], also plotted in Fig. 3.4h as comparison. The reason for this surprising behavior is not clear yet. Although one would expect that instead of the usual trivalent ions, the divalent ions of Bi or La could be present, measurements of Bi core levels in our samples are inconsistent with this hypothesis. One possibility

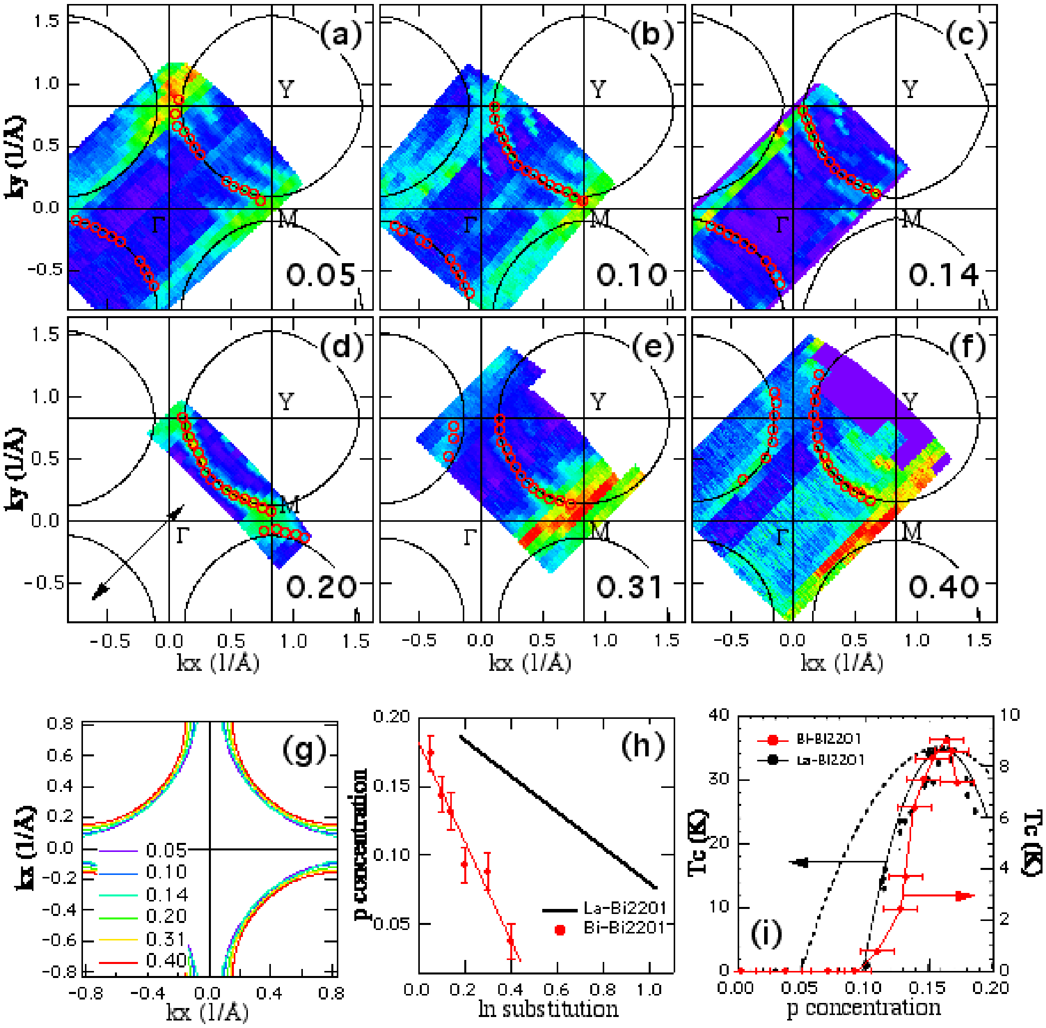

Figure 3.4: FS mapping of $Bi_2Sr_{2-x}Bi_xCuO_{6+\delta}$ at different Bi contents. (a)-(f) Plots of ARPES intensity integrated within $\omega = 0 \pm 12$ meV for $x = 0.05$, 0.1, 0.14, 0.2, 0.31, 0.4. The red circles are extracted from MDC peaks, and the lines are the tight-binding fits to the circles. All the samples are aligned along ΓY parallel to $\vec{A}$, as shown by the arrow in (d). (g) FS contours from tight-binding fits. (h) Doping effect induced by the substitution of Bi (dots, the thin line is the best linear fit) and La (solid line) measured by Hall measurements [6]. (i) Corresponding phase diagrams of Bi-Bi2201 and La-Bi2201, in comparison to a generic phase diagram of the high-T_c cuprates [7].

to explain this phenomenon is that the oxygen dopant concentration δ, which is not known precisely in these materials, increases with x, compensating the extra charge of the Bi^{3+} ion, and maintaining total charge neutrality $2\delta = p + x$. Spectroscopic evidence has led to a similar scenario for the electron-doped cuprates, where the Ce^{4+} dopant ions tend to form pairs with the extraneous oxygen ions [8].

In Fig. 3.4i, we construct the phase diagram of Bi-Bi2201 based on transport/susceptibility measurements [4] and the relationship of p vs x displayed in Fig. 3.4h. This phase diagram, when rescaled along the temperature axis, matches well with the one constructed from the Hall measurements of the La-Bi2201 [6]. We note that in both Bi and La substituted samples, T_c vanishes around 10% hole concentration, which is larger than the 5% critical value found in many cuprates [7]. This suggests that underdoping is not the only effect introduced by the $Sr^{2+} \rightarrow Bi^{3+}$ substitution. Beyond the chemical doping necessary to vary the carrier concentration in cuprates, a host of experiments have provided evidences that the ionic and electronic structures outside the CuO_2 planes have important effects on the low-energy electronic states and the superconducting properties [9–12]. In particular, the substitution of Sr^{2+} by Ln^{3+} (Ln = La, Pr, Nd, Sm, Eu, Gd, Bi) in $Bi_2Sr_{2-x}Ln_xCuO_{6+\delta}$ leads to a critical temperature that significantly depends on ion radius mismatch (Δr): at $x = 0.4$, $T_c \sim 30$K for La-substitution which has the smallest Δr, while $T_c \sim 0$K for Bi-substitution which has the largest Δr [10]. These results have been cited as evidence of strong dependence of T_c to apical site (A-site) disorder. However, our results suggest that this is not the complete story. As shown in Fig. 3.4h, at the fixed substitution level $x = 0.4$, the hole doping levels are different for La-Bi2201 ($p \sim 0.16$, optimally doped) and Bi-Bi2201 ($p \sim 0.05$, heavily underdoped). Nevertheless, there is a factor of 3 in terms of the maximum T_c's in these two systems, suggesting the superconducting properties of $Bi_2Sr_{2-x}Ln_xCuO_{6+\delta}$ are influenced by both charge underdoping and lattice disorder, the dual characters associated with chemical substitution.

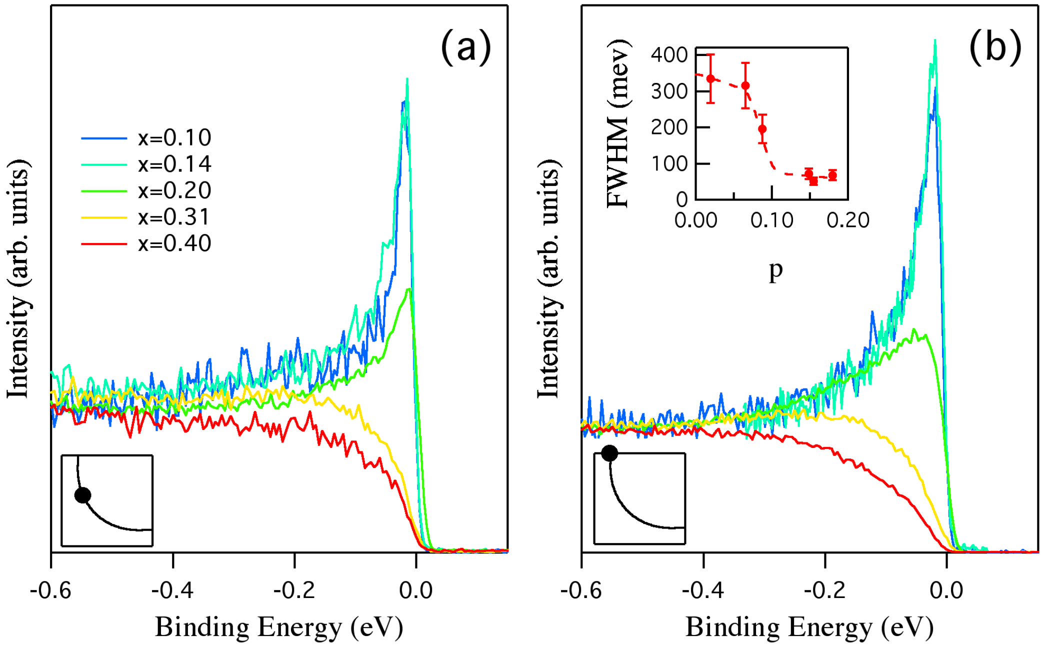

Figure 3.5: Comparison of EDC lineshape of Bi-Bi2201 at different Bi contents. (a) Near the node, and (b) near the antinode. The inset in (a) and (b) with black color show the k positions where those EDCs are taken. The inset in red color in (b) shows full-width-at-half-maximum (FWHM) of antinodal EDCs at K_F. The dashed line is a guide to eyes.

Another interesting phenomenon we observed is the dependence of the quasiparticle (QP) spectral coherence on the Bi content. In Fig. 3.5, we compare the near-nodal and antinodal energy distribution curve (EDC) lineshape for various Bi contents. Sharp EDC peaks are observed in both directions at low Bi substitution levels. The peak broadens as x increases, and the peak becomes totally incoherent in the heavily substituted samples. This loss of coherence is also accompanied by an opening of a soft energy gap characterized by the suppression of spectral weight in the vicinity of the Fermi energy (E_F). The crossover between the two regimes occurs around $x = 0.20$, which corresponds to a doping of $p \sim 0.1$, the superconducting-nonsuperconducting phase boundary at zero temperature. We plot the width of EDCs at k_F for the antinodal region in the inset of Fig. 3.5b. One clearly sees a significant linewidth broadening when $p < 0.1$, corresponding to $x > 0.2$. This may suggest that the superconductivity is closely correlated to the QP coherence. We also note that the opening of this soft gap first appears in the antinodal region and spreads out to the nodal one upon increasing substitution, as indicated in Fig. 3.5. A similar but smaller nodal gap has been also observed previously in several lightly doped high-T_c cuprates, and was attributed to disorder effect [13].

Perhaps the most surprising finding from our study is the observation of different antinodal pseudogap behaviors at low and high Bi contents. The temperature dependence of the symmetrized antinodal EDCs is given in Figs. 3.6a and b for $x = 0.2$ and $x = 0.4$ samples, respectively. The antinodal gap is filled in and disappears above

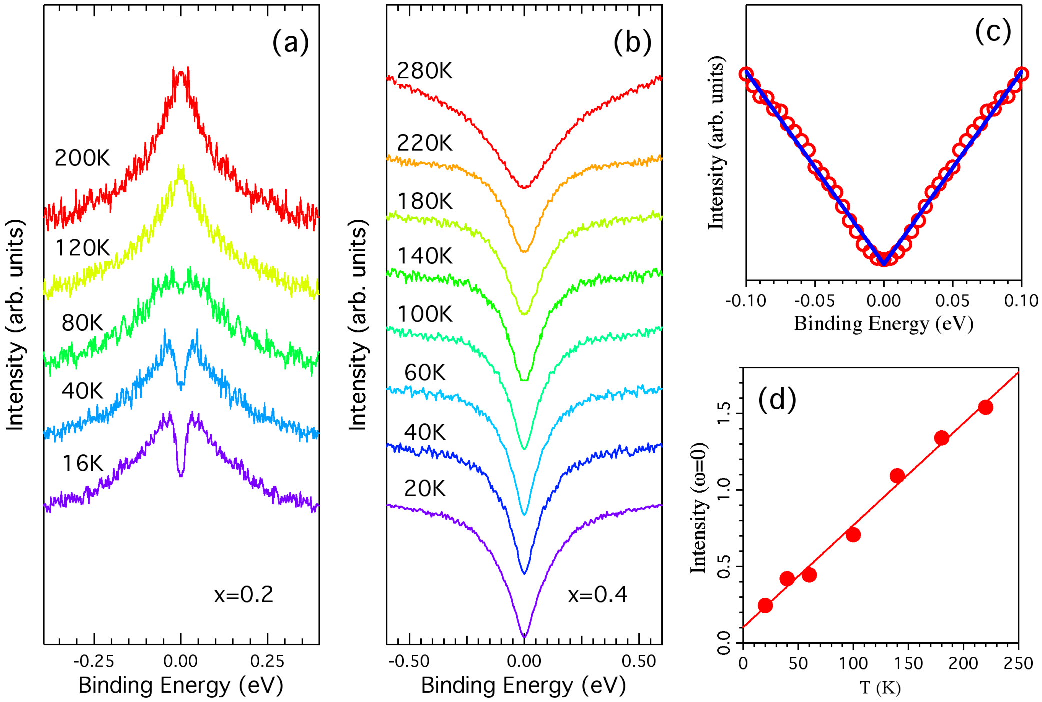

Figure 3.6: (a) Temperature dependence of symmetrized EDCs at K_F in the antinodal region for $x = 0.2$ sample, and (b) for $x = 0.4$ sample. (c) Zoom-in view of the 20K EDC shown in (b) near E_F and a linear fit to it. (d) Temperature dependence of EDC intensity at E_F (dots) and the corresponding linear fit (line) for $x = 0.4$ sample.

80 K for the $x = 0.2$ sample, similar to the conventional behavior of the pseudogap observed by STM for similar samples [14]. The larger gap of the $x = 0.4$ sample behaves differently in the following ways: (1) it lacks a well-defined spectral structure to define the value of gap, although the suppression of spectral intensity starts from ~ 0.2 eV; (2) while its overall spectral shape is little affected within the temperature range up to 280 K, the intensity at E_F is linearly proportional to temperature, as shown in Fig. 3.6d; (3) the spectral intensity is suppressed to zero at E_F linearly in energy at low temperature, as shown in Fig. 3.6c. This reminds us of the classical Coulomb gap (CG) behavior in strongly disordered two-dimensional systems [15], and suggest that the pseudogap in the underdoped regime has evolved into a Coulomb gap following the superconductor-insulator transition.

To test this finding, we performed transport measurements on the same samples to look for evidence of the Coulomb gap. The temperature dependence of the in-plane resistivity of $\mathrm{Bi_2Sr_{2-x}Bi_xCuO_{6+\delta}}$ at different Bi content x is plotted in Fig. 3.7 as the natural logarithm of resistivity versus $T^{-\frac{1}{2}}$. The superconductor-insulator transition around $x = 0.2$ is clearly visible. For $x > 0.2$, the resistivity curves show approximately linear behavior over a wider range of temperature, consistent with the classical hopping resistivity in the presence of a Coulomb gap, $\rho(T) = \rho_0 \exp(T_0/T)^{\frac{1}{2}}$, expected for a disordered insulating system with long-range Coulomb interaction [15]. Here $T_0 = e^2/\kappa\xi$ is the long-range Coulomb energy scale determined by the dielectric constant κ and the localization length ξ. From the slope of T-dependent curves in

Fig. 3.7a, we obtain T_0 and plot them in Fig. 3.7c (red dots). For the x=0.4 sample, $T_0 \sim 400$K, which explains qualitatively the soft gap in the antinodal spectrum visible even at $T = 280$K shown in Fig. 3.6b. Indeed, extrapolating the linear T-dependence of ARPES intensity at E_F (shown in Fig. 3.6d) allows a rough estimate of the crossover temperature $T^*_{CG} \sim 500$ K above which the suppression of the spectral weight ("gap") is completely filled. Thus the crossover temperature (T^*_{CG}) obtained from ARPES is consistent with T_0 derived from the resistivity, suggesting that the same Coulomb energy scale is involved in both ARPES and transport.

The ARPES spectra shown in Fig. 3.6b allows an estimate of the magnitude of the energy gap at the antinode for the x=0.4 sample, $\Delta \sim 0.19$ eV. This, combined with the derived value of $T_0 \sim 400$K for the same sample (see Fig. 3.7c), gives a ratio of $\Delta/T_0 \sim 5$. It is known from the theory of the classical Coulomb gap [15], $\Delta/T_0 = g_0(\xi)^2 T_0$ where g_0 is unperturbed density of states. A reasonable value of $g_0 \sim 2.1$ state/eV cell was provided by band theory for Bi2201 [16]. Taking $\xi \sim$ 8 unit cells, we estimate that the ratio predicted by the Coulomb gap theory to be ~ 5. This remarkable qualitative agreement between the experimental ratio and theoretical one strongly supports the Coulomb gap nature of the observed soft gap in the photoemission spectra. It is interesting to note that T_0 becomes smaller as the Bi content decreases and becomes zero as x becomes 0.2, the superconductor-insulator boundary revealed by the combined effects of underdoping and disorder. We caution here that the conventional Coulomb gap usually referred to the linear suppression of the density of states (DOS) in an isotropic system, not to the spectral function measured near the antinodal region of a highly anisotropic material. Nevertheless, the antinodal intensity dominates the DOS in the hole-doped cuprates due to the van Hove singularity.

A natural question to ask is how universal this Coulomb gap behavior is in the heavily underdoped high-T_c cuprates achieved by chemical substitution. To answer this question, we compared the antinodal EDC of the $x = 0.4$ sample with heavily underdoped $\mathrm{Bi_{2.1}Sr_2Ca_{1-x}Y_xCu_2O_8}$ ($T_c \sim 30$K) [17] and nonsuperconducting $\mathrm{Ca_{1.95}Na_{0.05}CuO_2Cl_2}$ (Na-CCOC) [18], as shown in Fig. 3.7b. We found that the lineshape of these different samples are very similar, characterized by the opening of a large soft gap and the absence of the QP peak.

Interestingly, as shown in the case of $\mathrm{Bi_{2.1}Sr_2Ca_{1-x}Y_xCu_2O_8}$ [17], the antinodal leading-edge gap was found to increase upon more underdoping, while the near-nodal gap seems to decrease and be proportional to T_c. This apparent gap dichotomy (or two-gap scenario) has been interpreted as evidence that the d-wave pairing gap opens along the FS arc around the node while the antinodal gap is a different type of gap that may not contribute to superconductivity [17]. However, with the appearance of a Coulomb gap in heavily substituted/underdoped samples, we raise another possibility, as summarized in the schematic phase diagram shown in Fig. 3.7c: upon increasing underdoping, the d-wave-like leading-edge gap region may be influenced or even truncated by the Coulomb gap region, which by itself is induced by the intrinsic

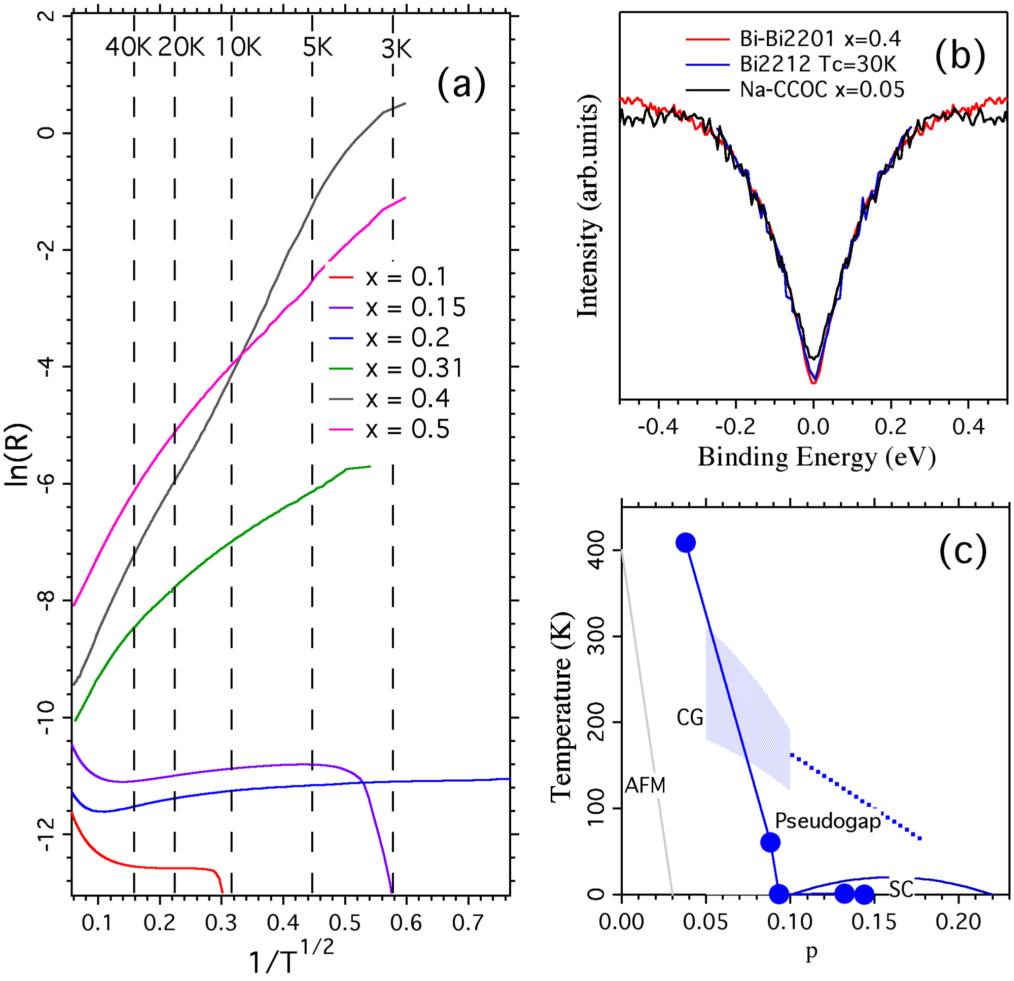

Figure 3.7: (a) Natural logarithm of resistivity versus $T^{-\frac{1}{2}}$ for samples x = 0.1, 0.15, 0.2, 0.31, 0.4 and 0.5. (b) Lineshape comparison of the antinodal EDCs in $Bi_2Sr_{1.6}Bi_{0.4}CuO_{6+\delta}$, $Bi_{2.1}Sr_2Ca_{1-x}Y_xCu_2O_8$ (from Ref. [17]) and $Ca_{1.95}Na_{0.05}CuO_2Cl_2$ (from Ref. [18]). (c) Qualitative phase diagram of $Bi_2Sr_{2-x}Bi_xCuO_{6+\delta}$.

disorder associated with chemical substitution. While this Coulomb gap region might push the onset of the superconducting phase to a higher doping level, as observed in the substituted Bi2201, it may also result in a spin glass phase often observed between the antiferromagnetic insulating phase and the superconducting state at low temperatures.

Bibliography

[1] Damascelli, A., Hussain, Z. and Shen, Z. -X., Rev. Mod. Phys. **75**, 473 (2003).

[2] K. Tanaka *et al.*, *Phys. Rev. B* **70**, 092503 (2004).

[3] A. Kanigel *et al.*, *Nature Physics* **2**, 447 (2006).

[4] H. Luo *et al.*, *J. Crystal Growth* **305**, 222 (2007).

[5] H. Ding *et al.*, *Phys. Rev. Lett.* **78**, 2628 (1997).

[6] Y. Ando *et al.*, *Phys. Rev. B* **61**, R14956 (2000).

[7] M.R. Presland *et al.*, *Physica C* **176**, 95 (1991).

[8] G. Riou *et al.*, *Phys. Rev. B* **69**, 024511 (2004).

[9] J.P. Attfield, A.L. Kharlanov, and J.A. McAllister, *Nature* **394**, 157 (1998).

[10] H. Eisaki *et al.*, *Phys. Rev. B* **69** 064512 (2004).

[11] K. McElroy *et al.*, *Science* **309**, 1048 (2005).

[12] P. Richard *et al.*, *Phys. Rev. B* **74**, 094512 (2006).

[13] K.M. Shen *et al.*, *Phys. Rev. B* **69**, 054503 (2004).

[14] M. Kugler *et al.*, *Phys. Rev. Lett.* **86**, 4911 (2001).

[15] A.L. Efros and B.I. Shklovskii, *J. Phys. C: Solid State Phys.* **8**, L49 (1975).

[16] M. S. Hybertsen and L. F. Mattheiss, *Phys. Rev. Lett.* **60**, 1661 (1988).

[17] K.Tanaka *et al.*, *Science* **314**, 1910 (2006).

[18] K. Shen *et al.*, *Science* **307**, 901 (2005).

Chapter 4

High Energy Kink

4.1 Introduction

Understanding the electronic structure and properties in strongly correlated systems, in particular in the high–T_c cuprates, has been a main focus in condensed matter physics over the past two decades. Unlike in simple metals and insulators, the presence of strong correlation makes the predictions of band calculations such as the LDA unreliable. Much of the theoretical understanding, based upon studies of Hubbard-like models, is the existence of strongly renormalized coherent quasi-particle excitations of a much reduced bandwidth *à la* Brinkman-Rice [1] and Gutzwiller wavefunctions [2], and large incoherent background of the Mott-Hubbard [3] type that extends to the bare band edge [4]. Both features have been ubiquitously observed in the cuprates, yet the precise description of the one-particle spectral function over the range of bare bandwidth provided by LDA remained incomplete due to the complexity of this many-body problem. The correlation-induced thermodynamic mass renormalization in the cuprate is ~ 3, which can be directly extracted from the renormalized Fermi velocity determined from angle-resolved photoelectron spectroscopy (ARPES) in the prototype $Bi_2Sr_2CaCu_2O_{8+\delta}$. Many ARPES measurements have been performed to determine the band dispersion in the high-T_c cuprates. Remarkably, the band dispersion for the quasiparticle excitations can only be traced up to ~ 350 meV, above which the band seems to disappear and the anticipated band bottom at the Γ (0,0) point has not been identified [5].

A recent ARPES on the undoped cuprate $Ca_2CuO_2Cl_2$ also found that the renormalized band is truncated around 350 meV, and the incoherent part at high energy seems to follow the bare band dispersion predicted by LDA [6]. It was suggested that the cause of this truncation is the antiferromagnetic fluctuations, with a characteristic energy scale of $2J$, where $J \sim 120 - 160$ meV is the superexchange coupling of the Cu-O square lattice. Many experiments has been performed on different materials, and many explanations are proposed, spinon-holon scenario [7], coupling to spin excitations [8], matrix element [9]. A lot of theoretical publications appears. The understanding is still under debate.

We performed a systematic APRES study on the complete band dispersion of various cuprates, including hole-doped $Pb_xBi_{2-x}Sr_2CuO_{6+\delta}$ and electron-doped $Pr_{1-x}LaCe_xCuO_4$. The most important of our findings is that the truncation energy scale of the coherence-incoherence crossover is *not* fixed around 350 meV, or $\sim 2J$, instead it is determined by and scales with the bare bandwidth. In the electron-doped cuprates, this crossover along $\Gamma - X$ occurs around $\sim$ 600 meV, much larger than the value (350 meV) in the hole-doped ones. At binding energies above the crossover, the incoherent part of the spectrum takes the form of a nearly vertical "dispersion" around a fixed crystal momentum k, and approaches the bare band bottom predicted by LDA. In addition, we observe for the first time the bottom of the renormalized band whose intensity is strongly suppressed. The complete determination of the coherent part of the occupied $\mathrm{Cu}3d_{x^2-y^2}$ band enables us to provide the tight-binding parameters and compare to the more realistic quasiparticle dispersion calculated from models with strong local correlation. We find that the renormalized dispersion obtained from the Gutzwiller projected wavefunction approach to the $t - J$ like models is a promising candidate for the observed low energy quasiparticle band.

4.2 Experiment Method

High quality single crystals of cuprates $\mathrm{Pb}_x\mathrm{Bi}_{2-x}\mathrm{Sr}_2\mathrm{CuO}_{6+\delta}$ (Pb-Bi2201), $\mathrm{Bi}_2\mathrm{Sr}_2\mathrm{CaCu}_2\mathrm{O}_{8+\delta}$ (Bi2212), and $\mathrm{Pr}_{1-x}\mathrm{LaCe}_x\mathrm{CuO}_4$ (PLCCO) were prepared by the the traveling solvent floating zone method, and some were annealed subsequently. ARPES experiments were performed at the Synchrotron Radiation Center, WI, and the Advanced Light Source, CA. High-resolution undulator beamlines and Scienta analyzers with a capability of multi-angle detection have been used. The energies of photons were carefully chosen in order to enhance certain spectral features. The energy resolution is $\sim$ 10 - 30 meV, and the momentum resolution ~ 0.02 Å^{-1}. All the samples were cleaved and measured *in situ* in a vacuum better than 8×10^{-11} $Torr$ at low temperatures (14 - 40 K) on a flat (001) surface, and all the spectra shown below have been reproduced on multiple samples.

4.3 ARPES Results

We start with a set of spectra along $\Gamma - X$ on a hole-doped $\mathrm{Pb}_x\mathrm{Bi}_{2-x}\mathrm{Sr}_2\mathrm{CuO}_{6+\delta}$ (overdoped $T_c \sim$ 7K), as shown in Fig. 1. The reason we choose this material is that the Pb substitutions remove the superlattice modulation in Bi-O plane, which often complicates ARPES spectra [10]. The spectra were taken along $\Gamma - X$ in the second Brillouin zone (BZ) using 57-eV s-polarized ($\vec{A} \parallel \Gamma X$) photons to enhance various features at high binding energy (> 350 meV). In Fig. 1a, one can easily follow the dispersive band at low energy (< 350 meV). This band is the well-know Zhang-Rice singlet [11], with the predominant Cu3$d_{x^2-y^2}$-O2$p_{x,y}$ antibonding orbital. While the Fermi vector k_F is almost the same as the one predicted by LDA, as shown in Fig. 1d, its dispersion velocity v_k ($\sim$ 2.1 eVÅ) is much smaller than the LDA value ($\sim$ 5.2 eVÅ) [12], consistent with previous ARPES results [10, 13, 14]. Note that the Fermi velocity v_F ($\sim$ 1.6 eVÅ) at k_F is even smaller due to a further renormalization by the observed nodal kink at $\sim$ 70 meV [15, 16], which is difficult to visualize at the large energy scale in Fig. 1. At higher binding energy (> 350 meV), the spectrum becomes

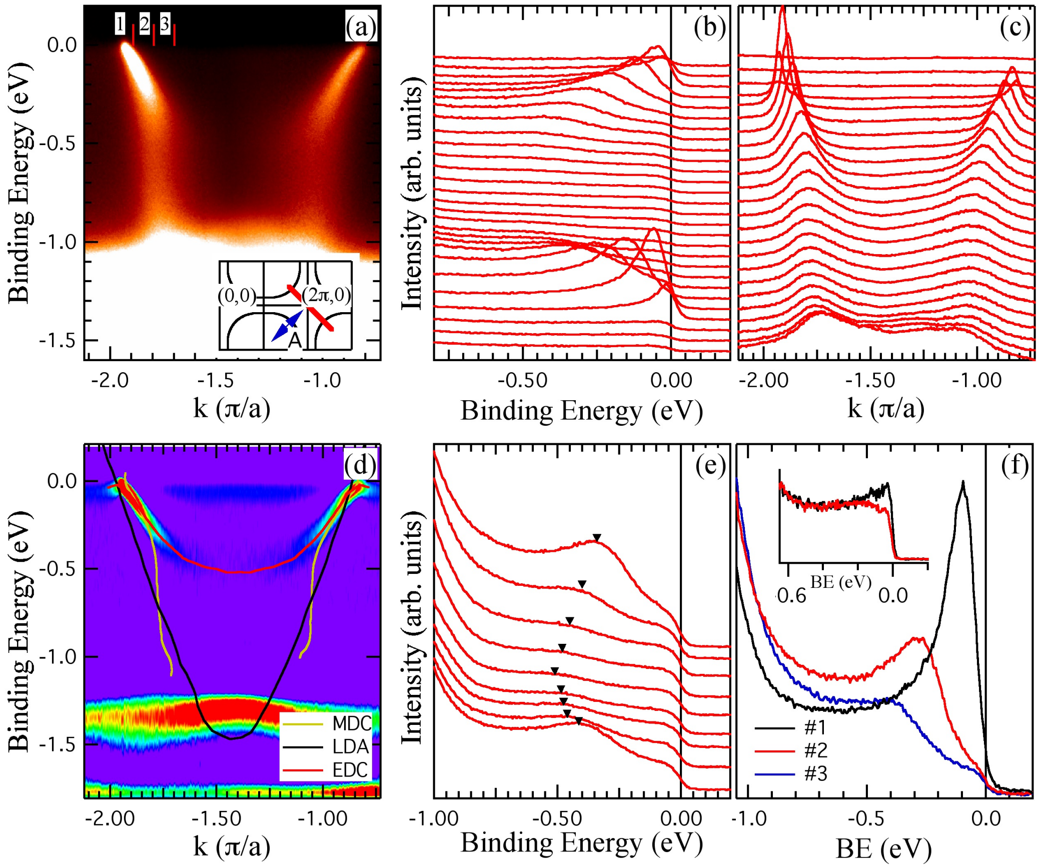

Figure 4.1: Dispersion of coherent and incoherent bands along $\Gamma - X$ in Pb-Bi2201 measured at 20K using 57-eV s-polarized photons. (a) - (d) Plots of E-k intensity, EDCs, MDCs, and the second derivative intensity, respectively. The inset in panel (a) displays the measurement locations in BZ. In panel (d), three extra lines of dispersion extracted from EDCs (red), MDCs (yellow), and LDA calculation (black) are also superimposed for the comparison purpose. (e) Magnified plot for EDCs near Γ. (f) Comparison of three EDCs at the k-locations labeled as #1 to #3 in Fig. 1a. The inset shows two EDCs of Bi2212 at the similar k-locations as #1 and #2, but using p-polarized photons.

ill-defined. While the intensity plot (Fig. 1a) seems to indicate that the spectra abruptly "dive" almost vertically from 350 meV to at least 1 eV, this diving behavior does not expressed itself as a peak in the energy distribution curves (EDCs) (Fig. 1b). Instead, an enhancement in the EDC background is observed at the k-location of the dive around $(\pi/4, \pi/4)$ and equivalent k points in other BZs, as shown in Fig. 1f where the EDC at the dive location (# 2, as marked in Fig. 1a) has a higher background than its neighboring EDCs (*e.g.*, # 1 and # 3). The diving behavior is reflected more clearly in the momentum distribution curves (MDCs), as shown in Figs. 1d where the MDCs seem to maintain their peak shape. Since the dive completely loses the peak (or pole) structure in energy, strictly it is no longer a band. Nevertheless, it is likely the incoherent part of the Cu$3d_{x^2-y^2}$-O$2p_{x,y}$ (or ZRS) spectrum, since it maintains the $d_{x^2-y^2}$ symmetry. We have verified this symmetry, as shown in the inset of Fig. 1f, where both the coherent band and the dive are suppressed by p-polarized light ($\vec{A} \perp \Gamma X$). This is due to a well-known ARPES selection rule [17]. In addition, we have also observed that the intensity ratio between these two features is roughly a constant when we change s and p polarization components, supporting that the dive is the incoherent part of the band.

So far we have shown that the coherent ZRS band disperses to a certain energy ($\sim$ 350 meV) and then abruptly switches to the incoherent part at the higher energies. However, if we take a closer look at the EDCs in the vicinity of Γ, we observe the smooth continuation of the coherent band, which reaches the bottom around 0.5 eV at Γ, as shown in Fig. 1e. This is the long-sought-after renormalized band bottom, and the reason we can observe it for the first time is due to several combined factors such as the superlattice free sample, a proper photon energy, and the second BZ, all of which enhance the intensity of the high-energy features. We note that the coherent band starts to lose its intensity at the same energy where the incoherent diving pattern begins to form, indicating a weight transfer between the coherent and incoherent parts. The bottom of the coherent band can be also visualized, as shown in Fig. 1d, from the second derivative of the intensity with respect to energy which enhances broad horizontal features. In Fig. 1d, we compare the dispersion of the coherent band with the calculated one from LDA, along with the dispersion extracted from MDCs. It is clear that the coherent band, with a well-defined parabolic shape, is highly renormalized, and the vertical feature is likely the incoherent part, which approaches the bottom of the bare band.

We have observed very similar behaviors of the coherence-incoherence crossover in the bilayer system $Bi_2Sr_2CaCu_2O_{8+\delta}$, except the superlattice in this material makes it difficult to observe the bottom formation of the coherent band at Γ. Like in Pb-Bi2201, the incoherent part in Bi2212 deviates from the coherent part around 350 meV, and approaches almost vertically the bare band bottom around 1.5 eV. There may have more than one band at the bare band bottom, as predicted by LDA calculations. Some sharp features have been observed around 1 - 1.5 eV in $YBa_2Cu_3O_{7-x}$ [18]. Since the 350 meV energy scale of the coherence-incoherence crossover has been at-

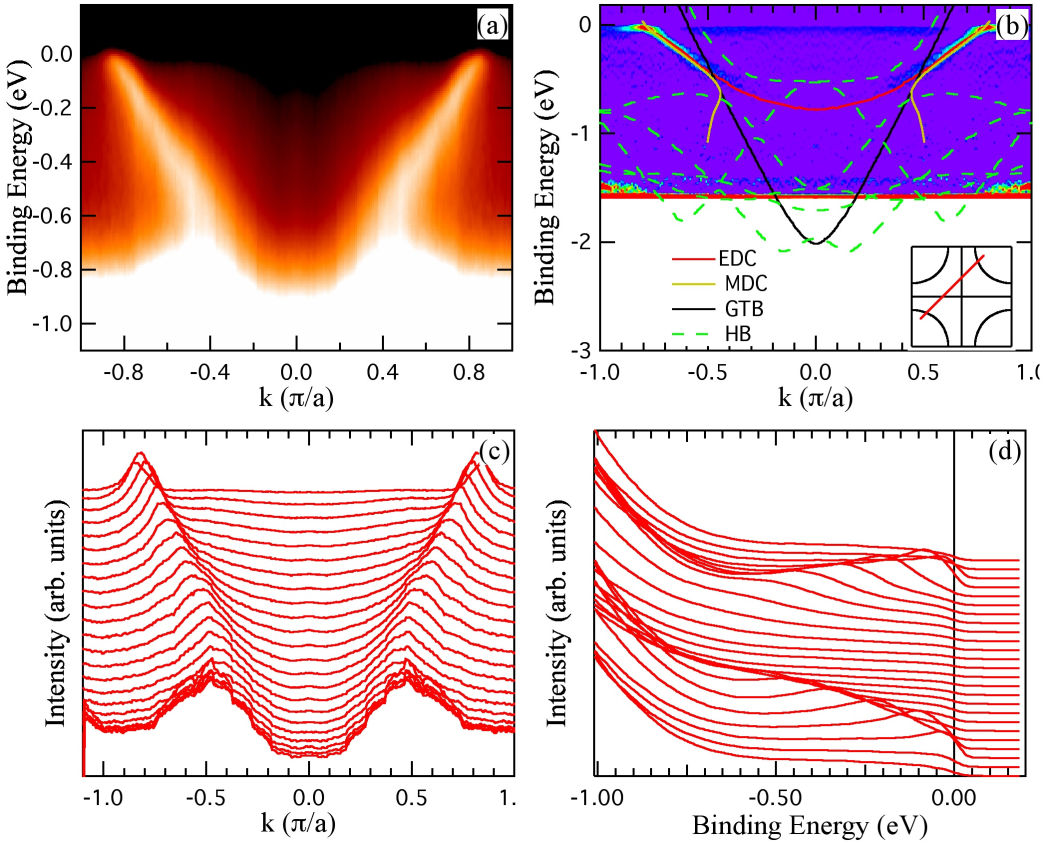

Figure 4.2: Dispersion of the coherent and incoherent bands near $\Gamma - X$ in PLCCO measured at 40 K using 22-eV photons. (a) - (d) Plots of E-k intensity, second derivative intensity, EDCs, and MDCs, respectively. The inset in panel (b) displays the measurement locations in BZ. The superimposed curves in panel (b) are the extracted EDC positions (red), fitted MDC positions (yellow), non-hybridized LDA band (solid black) and hybridized LDA bands (dashed green) along $\Gamma - X$.

tributed to the antiferromagnetic fluctuations whose characteristic energy scale $2J$ has a similar value [6], it is natural to check if a similar coherence-incoherence crossover exists in the electron-doped cuprates. We have searched for this crossover on various electron-doped cuprates, and the main results are presented in the following two figures.

We first show, in Fig. 2, the dispersion of the electron-doped cuprate $\mathrm{Pr_{0.88}LaCe_{0.12}CuO_4}$ ($T_c \sim 23$ K) near $\Gamma - X$ using 22-eV p-polarized photons. Since the band intensity exactly along $\Gamma - X$ is highly suppressed due to the selection rule mentioned above, we choose to display the dispersion along the parallel direction slightly away from the $\Gamma - X$ direction, as indicted in the inset of Fig. 2b. A quick examination of the plots of Fig. 2 reveals a major difference to the hole-doped materials: the coherent band in PLCCO extends to a much higher binding energy. The separation of the incoherent part occurs around 0.6-0.7 eV, which also forms a diving pattern at higher binding energy, as seen in both the intensity plot in Fig. 2a and the MDCs plot in Fig. 2c. We note that the diving pattern appears to be shorter than the one in the hole-doped cuprates. We believe that this is due to the hybridization between the $\mathrm{Cu}3d_{x^2-y^2}$ band and some other bands, as predicted by LDA calculations [19] and shown in Fig. 2b (dashed green curves). The bare $\mathrm{Cu}3d_{x^2-y^2}$ band, while not mixing with those bands, reaches the bottom around 2.1 eV, as indicted in Fig. 2b (solid black curves) [20]. In comparison, the coherent part has its band bottom around 0.8 eV, indicating a mass renormalization of 2.5, similar as in the hole-doped case.

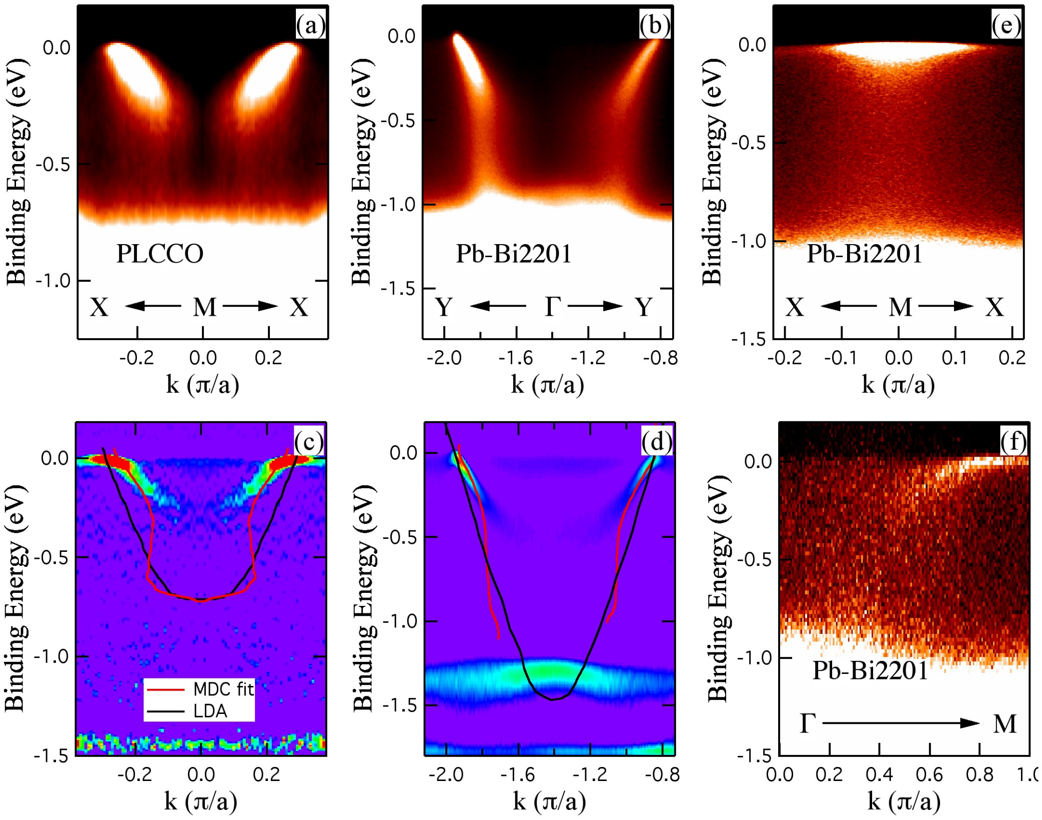

Figure 4.3: Comparison of band dispersion between PLCCO and Pb-Bi2201. (a) - (b) E-k intensity plots for $M-X$ in PLCCO using 22-eV photons and $\Gamma-X$ in Bi2201 using 57-eV photons, respectively. (c) - (d) Corresponding second derivative plots for panels (a) and (b), respectively. MDC dispersion (red lines) and bare band from LDA (black lines) are superimposed to the plots in panels (c) and (d). (e) - (f) E-k intensity plots along $M-X$ and $\Gamma-X$ in Bi2201.

The different energy scale of the coherence-incoherence crossover in the electron-doped cuprates, as observed in PLCCO and confirmed in other electron-doped materials, such as $\mathrm{Pr}_{2-x}\mathrm{Ce}_x\mathrm{CuO}_4$ and $\mathrm{Nd}_{2-x}\mathrm{Ce}_x\mathrm{CuO}_4$, argues strongly against the antiferromagnetic scenario. Instead, the same mass renormalization ratio in both cases suggests that this energy scale may be related to the bare bandwidth. This is also true in the electron-doped material along another high-symmetry direction, $M - X$, as can be seen in Fig. 3. It is well known that the van-Hove saddle point shifts to a much higher binding energy (~ 0.4 eV) in the electron-doped cuprates [21, 22]. Over the wide energy range, the $\mathrm{Cu}3d_{x^2-y^2}$ band dispersion along $M - X$ in PLCCO has many similarities to the band along $\Gamma - X$ in Bi2201, as shown in Fig. 3. The coherent part along $M - X$ in PLCCO, while being quite broad due to the possible stronger interactions near the antinode, extends to an energy scale (~ 0.25 eV) when the incoherent part takes a dive around $k \sim (\pi, \pi/6)$. The bottom of the coherent part at M is estimated to be ~ 0.3 eV, and the bare band position at M is calculated by LDA to be ~ 0.7 eV. For comparison, we draw both intensity plot and second derivative plot of Pb-Bi2201 in the left panels of Fig. 3 in a slightly reduced energy scale. We also notice that there is a small kink at ~ 70 meV along $M - X$ in PLCCO, which resembles the well-know and much-debated nodal kink in the holed-doped cuprates [15, 16]. We caution that the origin of the antinodal kink in PLCCO may not be the same as the antinodal one in the hole-doped case, and call for more systematic studies.

We have measured band dispersion along many directions in the BZ for various hole- and electron-doped cuprates. In Fig. 4, we summarize our main results as a comparison between the coherent band dispersion and the bare band dispersion predicted by LDA along several high-symmetry directions, for both Pb-Bi2201 ($T_c \sim$ 7 K) and PLCCO ($T_c \sim$ 23 K) samples. We also use the effective tight-binding band to fit the coherent dispersion, using the standard formula as in previous work [5]. Since ARPES only measures the occupied side, we adapt the previous method [5] by choosing the unoccupied band top at X (π, π) in such a way that it maintains the same band renormalization ratio ($\sim$ 2.5) as the occupied side. We use the six free parameters (t_0 to t_5) with t_0 being the chemical potential, t_1 the nearest neighboring hopping term, and t_2 to t_5 the higher order hopping terms. The numeric values of these parameters are also listed in Fig. 4. The large difference of t_0 ($\sim$ 0.4 eV) between the two systems indicates a large chemical shift from the hole doped side to the electron doped side, which is likely the main cause of the downshift of ($\sim$ 0.4 eV) of the van Hove singularity in the electron-doped cuprates.

4.4 Discussion

We have determined by ARPES the complete low energy quasiparticle dispersion and elucidated its unusual evolution to the high energy incoherent background in both hole- and electron-doped cuprates. The reduction of the bandwidth from its bare value is most likely the result of strong local correlations that frustrate the kinetic energy. This is overall consistent with the Gutzwiller projected wavefunction

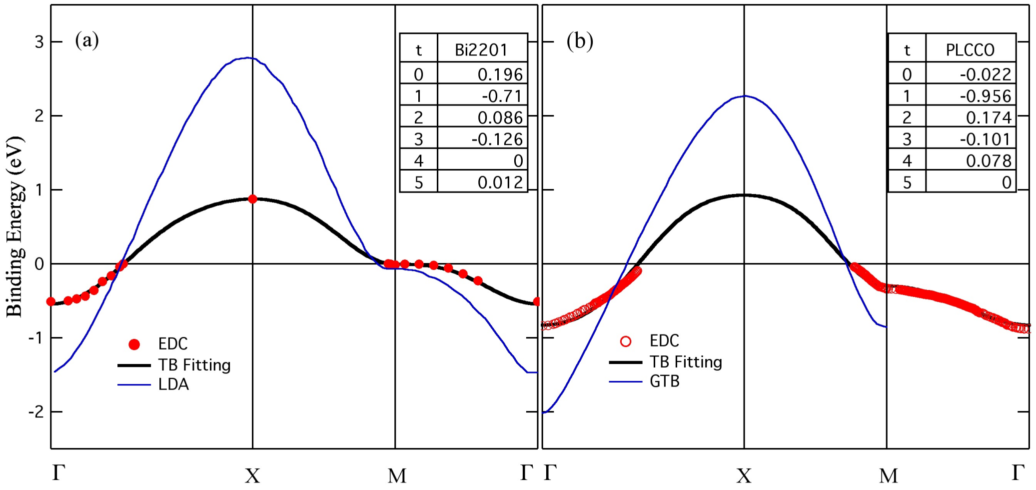

t	Bi2201
0	0.196
1	-0.71
2	0.086
3	-0.126
4	0
5	0.012

t	PLCCO
0	-0.022
1	-0.956
2	0.174
3	-0.101
4	0.078
5	0

Figure 4.4: Summary of coherent band dispersion along three principle directions (Γ-X, X-M, and M-Γ) for hole- and electron-doped cuprates. (a) - (b) Measured coherent band position (red dots), tight-binding fit (black solid line), and LDA band dispersion (blue dashed line) in Pb-Bi2201 and PLCCO, respectively. The inserted tables are the obtained fitting parameters.

approach to simple models of doped Mott insulators [23]. Detailed comparisons would require measurement of the doping dependence of the renormalized bandwidth, which is more difficult to determine due to the doping dependent shift of the chemical potential. More systematic studies are needed to clarify this issue. Most surprisingly, we find that the energy scale associated with the coherence-incoherence crossover is determined by a fraction of the bare band bottom energy and is in general different from the antiferromagnetic exchange energy $2J$, ruling out the latter as the main cause of quasiparticle decoherence at *high* binding energies. Moreover, it appears more universal that the incoherent spectrum beyond the decoherence energy takes a vertical dive with a nearly fixed k, approaching the bottom of the bare band in what seems to be the "cheapest" way for the renormalized quasiparticles to return to their bare form. The origin of these unexpected behaviors is largely unknown and demands more understanding of the interplay between the coherent quasiparticle and collective excitations and the dominant incoherent processes in the spectral function, which has been one of the central challenges in the physics of strong correlations.

Bibliography

[1] W. Brinkman and T.M. Rice, Phys. Rev. B **2**, 4302 (1970).

[2] M.C. Gutzwiller, Phys. Rev. Lett. **10**, 159 (1963).

[3] J. Hubbard, Proc. R. Soc. London A **276**, 238 (1963); **277**, 237 (1964);**296**, 82 (1967).

[4] Z. Wang, Y. Bang, and G. Kotliar, Phys. Rev. Lett. **67**, 2733 (1991).

[5] M.R. Norman, M. Randeria, H. Ding, and J.C. Campuzano, Phys. Rev. B **52**, 615 (1995).

[6] F. Ronning *et al.*, Phys. Rev. B **71**, 094518 (2005).

[7] J. Graph *et al.*, Phys. Rev. Lett. **98**, 067004 (2007).

[8] T. Valla*et al.*, Phys. Rev. Lett. **98**, 167003 (2007).

[9] D. Inosov *et al.*, Phys. Rev. Lett. **99**, 237001 (2008).

[10] H. Ding *et al.*, Phys. Rev. Lett. **76**, 1533 (1996).

[11] F.C. Zhang and T.M. Rice, Phys. Rev. B **37**, 3759 (1988).

[12] M.S. Hybertsen and L.F. Mattheiss, Phys. Rev. Lett. **60**, 1661 (1988); H. Krakauer and W.E. Pickett, Phys. Rev. Lett. **60**, 1665 (1988).

[13] D.S. Dessau *et al.*, Phys. Rev. Lett. **71**, 2781 (1993).

[14] T. Valla *et al.*, Phys. Rev. Lett. **85**, 828 (2000).

[15] T. Valla *et al.*, Science **285**, 2110 (1999).

[16] A. Lanzara *et al.*, Nature **412**, 510 (2001).

[17] M.R. Norman *et al.*, Phys. Rev. B **52**, 15107 (1995).

[18] C.G. Olson *et al.*, J. Phys. Chem. Solids **56**, 1879 (1995).

[19] S. Massida *et al.*, Physica C **157**, 571 (1989).

[20] M.M. Korshunov *et al.*, Phys. Rev. B **72**, 165104 (2005).

[21] D.M. King *et al.*, Phys. Rev. Lett. **70**, 3159 (1993).

[22] T. Sato *et al.*, Science **291**, 1517 (2001).

[23] P.W. Anderson *et al.*, J Phys. Condens. Matter **16** R755, (2004).

[24] J. Graf *et al.*, *cond-mat*/0607319.

[25] B.P. Xie *et al.*, *cond-mat*/0607450.

[26] T. Valla *et al.*, *cond-mat*/0610249.

Chapter 5

Superconducting gap and pseudogap in $La_xBi_2Sr_{2-x}CuO_{6+\delta}$

Pseudogap phase observed in underdoped high-Tc materials is the most unconventional phenomenon, characterized with a normal state pseudogap in the single particle excitation spectrum below a temperature T^*. Pseudogap was observed by ARPES on $Bi_2Sr_2CaCu_2O_{8+\delta}$ [1, 2]. The origin and how pseduogap gap is related to superconductivity are still under debate now. Two scenarios are proposed: one-gap scenario, pseudogap is formed through d-wave paring without superconduting phase coherence. As T goes below T_C, pairs become phase coherent and superconductivity builds [3–5]; two-gap scenario attributes pseudogap phase as a competing order. Recent ARPES experiments observed a large antinodal gap associated with pseudogap and a smaller nodal gap associated with superconductivity through k dependence, temperature dependence and doping evolution [6–8]. To resolve this question, detailed high resolution ARPES were performed on $La_xBi_2Sr_{2-x}CuO_{6+\delta}$, one advantage of this material is that high quality crystals is available over a wide doping range; the other advantage is that the availability of a atomically flat surface because BiO layers of crystal are bond by weak Van De Waals force, this is important for momentum resolution. Our results shows that pseudogap and supeconducting phase may coexist in the underdoped regime, two kinds gaps(a small gap and a large gap) were observed at antinodal region by ARPES and in real space by STM on almost optimal-doped $La_{0.4}Bi_2Sr_{1.6}CuO_{6+\delta}$. Temperature dependence shows very different behaviors for those two gaps. We show that the small gap observed below T_C is associated with superconductivity and the large gap which persists to T_C is associated with short range charge ordering. Superconductivity and charge ordering are driven by similar mechanism [18]. Surprisingly psedogap is also observed in overdoped samples.

5.1 Experiment Method

High quality single crystals of cuprates $La_xBi_2Sr_{2-x}CuO_{6+\delta}$were prepared by the the traveling solvent floating zone method, and some were annealed subsequently. ARPES experiments were performed at the Synchrotron Radiation Center, WI, and the ARPES group in Tohoku University. . High-resolution undulator beamlines and Scienta analyzers with a capability of multi-angle detection have been used. The energies of photons were carefully chosen in order to enhance certain spectral features.

The energy resolution is $\sim$ 10 - 30 meV, and the momentum resolution ~ 0.02 Å^{-1}. High energy resolution ARPES were perform with Xe lamp, the energy resolution were achieved at 4 meV at the photon energy 8.5 eV. All the samples were cleaved and measured *in situ* in a vacuum better than 8×10^{-11} $Torr$ at low temperatures (5 - 20 K) on a flat (001) surface, and all the spectra shown below have been reproduced on multiple samples.

5.2 ARPES Results

5.2.1 Fermi surface mapping

The intensity map of ARPES intensity at E_F is a direct illustration of Fermi surface. Fermi surface mappings of $\mathrm{La_{0.4}Bi_2Sr_{1.6}CuO_{6+\delta}}$and $\mathrm{La_{0.1}Bi_2Sr_{1.9}CuO_{6+\delta}}$at T = 10K are shown in Figure 5.1a and c. The intensity map is averaged within $\omega \pm 10$ meV window, which is a direct measurement of Fermi surface. We can see a large Fermi surface around Y(π, π) with stronger intensity around nodal region and beyond some k position close to antinodal region intensity becomes much weaker. This is not just because of the opening of gap but because of the loss of intensity of quasi-particle peak. To see this more clearly, EDCs along Fermi surface are plotted in Figure 5.1b and d. The k positions defined by the loss of QP peak are plotted as red lines in Figure 5.1a and c. The Fermi surface are divided into two regions in k space, nodal region with strong QP peaks and antinodal region with weak QP peaks. We

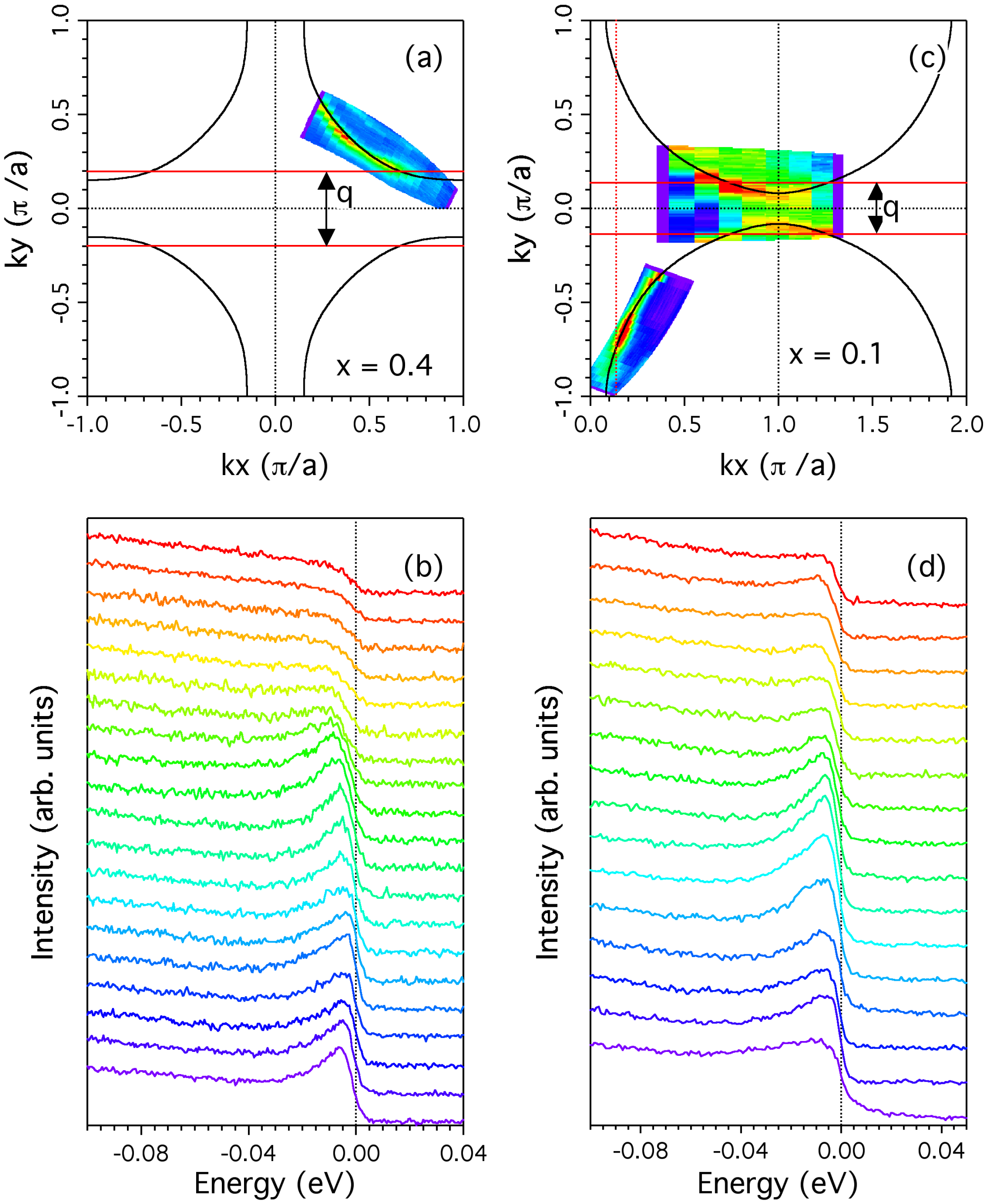

Figure 5.1: (a)-(b) Fermi surface mapping and EDCs along FS of $La_{0.4}Bi_2Sr_{1.6}CuO_{6+\delta}$. (c)-(d) Fermi surface mapping and EDCs along FS of $La_{0.1}Bi_2Sr_{1.9}CuO_{6+\delta}$. Intensity map is averaged within $\omega \pm 10$ meV window. The mapping is measured on Xe lamp with hv = 8.5 eV. The black line is a tight binding fit.

know that the opening of superconducting gap will push the intensity to high binding energy but will not cause QP peak loss. One possible scenario may be due to matrix element, which may affect photoemission intensity. The same result from different photon energy and geometry alignment rule out this possibility. The nodal region Fermi surface actually defines an arc.

EDC spectra at k_F can be symmetrized to remove the Fermi function effect, the results of $La_{0.4}Bi_2Sr_{1.6}CuO_{6+\delta}$are shown as in Figure 5.2a, the k positions are indicated by the circle with the same color in Figure 5.2b. The gap can be extracted from those symmetrized EDCs through the separation of the peaks. For those EDCs with peaks, the method of spectra function fitting [9] works well, while for those EDCs without a peak, gap value is extracted by the crossing point of those two straight lines drawn at low binding and high binding energies. The gap is plotted in Figure 5.2b, a pure d-wave fitting agrees well with the data, giving maximum gap $\Delta = 13.25$ meV. Earlier experiments [7] on $Bi_{2-y}Pb_ySr_{2-x}La_xCuO_{6+\delta}$with similar T_C showed similar results at nodal region but very different results at antinodal region: (i) a much larger antinodal gap ~ 35 meV is observed both below and above T_C; (ii) k dependence of low temperature gap shows a non-pure d-wave shape. One possible scenario is that two gap coexist at antinodal region. The large gap or pseudogap truncates Fermi surface and form a Fermi arc in the nodal region. However the pseudogap is a kind of soft gap, the E_F intensity at anitnodal region is suppressed but not zero. Below T_C, at nodal region pairing gap forms and superconducting peak

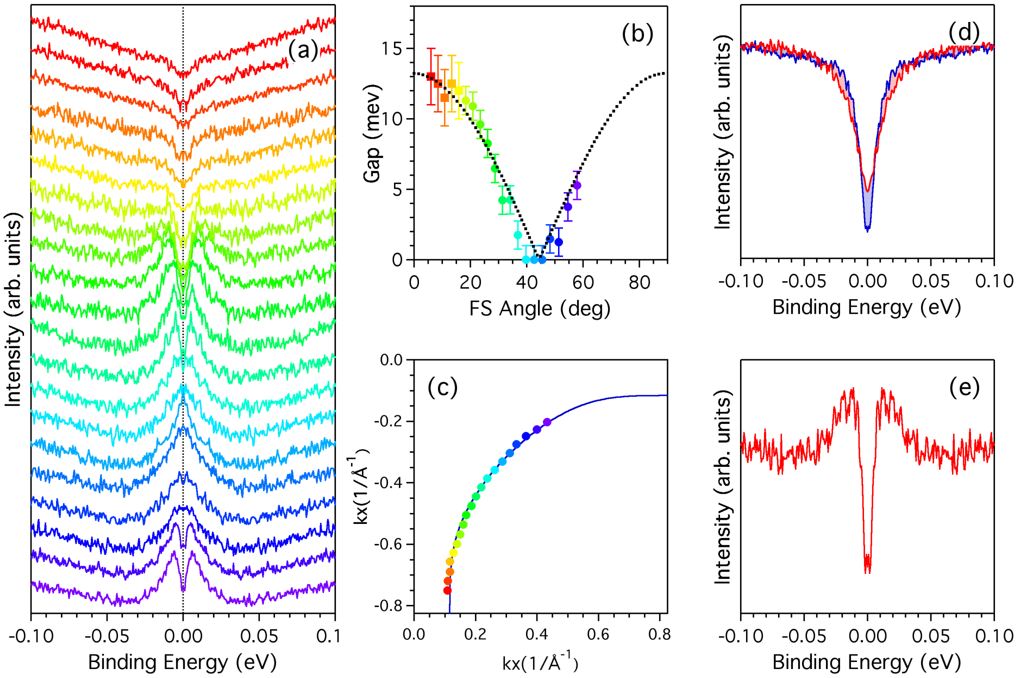

Figure 5.2: Superconducting gap of $La_{0.4}Bi_2Sr_{1.6}CuO_{6+\delta}$. (a) Symmetrized EDCs along Fermi surface. (b) d-wave-like superconducting gap. The dotted line is pure d-wave fitting. (c) The k position of symmetrized EDC in panel (a). The line is a tight binding fit. (d) Antinodal spectrum below and above T_C. (e) Antinodal spectra at 5K divided by 40K.

is strong because of high intensity at E_F, while at antinodal region, pairing gap forms and only weak superdoncuting peak builds because of the suppression of density of states. This is exactly what we observed in Figure 5.2d by comparing the spectrum below and above T_C. The spectra(red) above T_C shows a larger soft gap and finite intensity at E_F. Below T_C, the spectra has less intensity at E_F but more intensity at higher binding energy, this is the opening of a superconducting gap inside a soft pseudogap. A detailed check shows that the shadow area at low and high binding energy are exactly the same. By dividing the spectra at 5K by 40K, a clear coherent peak is observed shown in Figure 5.2e. This is the same as the results measured with high resolution synchrotron measurement [13], which has been explained by coupling to a bosonic mode. The discrepancy from $Bi_{2-y}Pb_ySr_{2-x}La_xCuO_{6+\delta}$may be due to different samples, Pb is introduced to remove the superlattice. However, Pb may also introduce other effects. Further study may be needed to resolve this.

STM data clearly show two gaps on the same sample [11], a small gap and a large gap. The large gap is close to the value of the antinodal pseudogap observed by ARPES; the small gap is close to the gap at arc tip. STM measures a k averaged spectrum, which has similar gap to arc tip because of the low intensity of antinodal region. Early STM did observed some form of short-range ordered checkerboard patterns in underdoped $Bi_2Sr_2CaCu_2O_{8+\delta}$ [12], Ca-xyochloride [13], and Pb-La-Bi2201 [14]. Fourier transform revealed a non-dispersive glassy charge order with corresponding wave vector $q = 2\pi/(5 \pm 1)a_0$ in the (0, π) direction. The q vector drawn between two adjacent arc tip points observed by ARPES gives the value $q = 2\pi/(5.2 \pm 0.7)a_0$, consistent with STM result. So the large gap observed at the antinodal region and STM is attributed to charge density wave(CDW). Two gaps are found to coexist at the anitnodal region. The small SC gap attributes to the superconductivity while the large pseudogap attributes to CDW.

$La_{0.1}Bi_2Sr_{1.9}CuO_{6+\delta}$was measured under similar condition and the results are shown in Figure 5.6. Sharp peaks are clearly seen at the nodal region, and become weaker from the node to the antinode. However, the peaks still exist even at the antinodal region. A drop of peak weight can still can seen clearly that the k space can be divided into the nodal region and the antinodal region. From Figure 5.1c, we can see that the antinodal region of $x = 0.1$ sample is much smaller than the one in x = 0.4 sample,which means a weaker CDW. Another evidence of weaker CDW is from a smaller pseudogap and higher intensity at E_F above T_C shown Figure5.6c. Because of the higher intensity at E_F, below T_C strong superconducting peaks are observed. The q-vector from the Fermi surface in Figure 5.1 is about $2\pi/(7.3 \pm 0.7)a_0$, corresponding spatial periodicity $\sim$ 26 Å. Since the CDW coherence length is short and approximately 10 $\sim$ 15 Å, so the large periodicity is not likely sustainable. This can also explain why the no folded band is observed by ARPES Fermi surface mapping. With more hole carriers in over doped materials, the kinetic motion is enhanced. So no clear CDW pattern is observed at this doping and the large CDW pseudogap is strongly suppressed. The weak pseudogap gap in the overdoped samples could arise

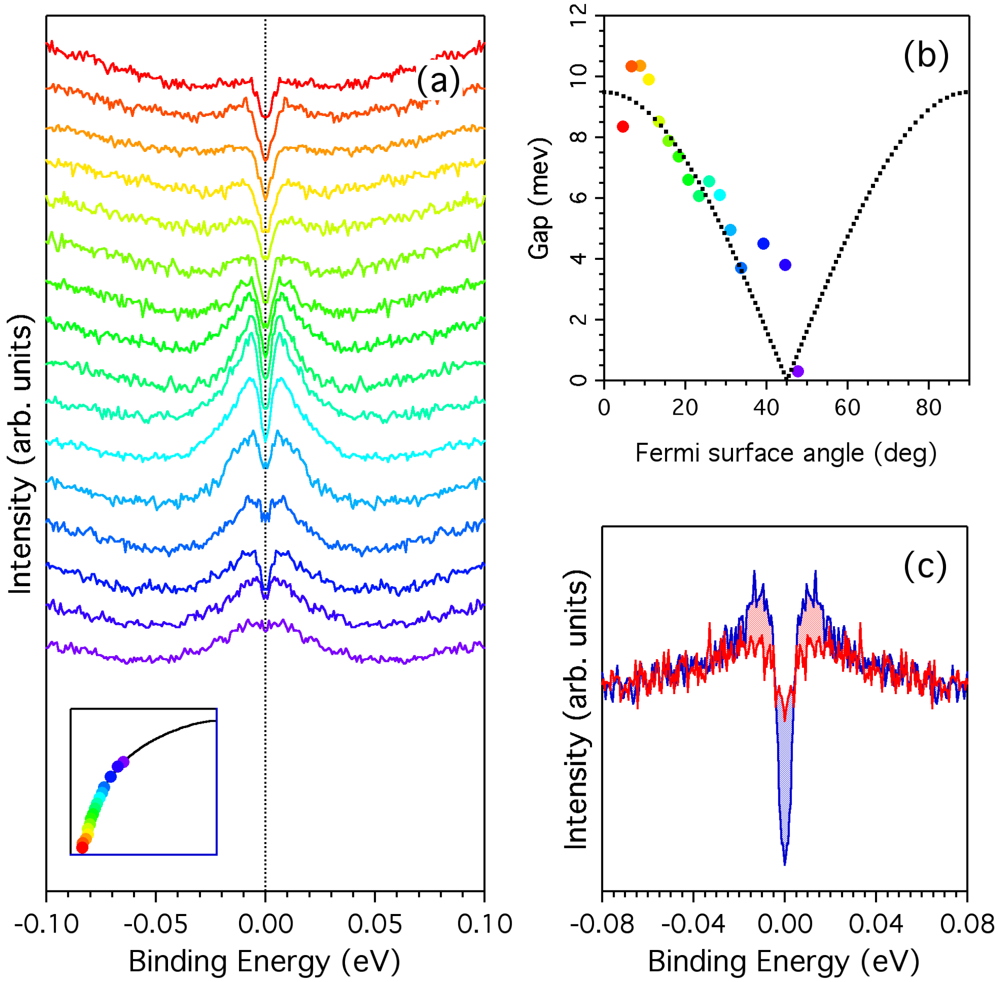

Figure 5.3: $La_{0.1}Bi_2Sr_{1.9}CuO_{6+\delta}$. (a) Symmetrized EDCs along Fermi surface at $T = 10$ K. Inset shows the k position where the spectra are taken. (b)Gap extracted from symmetrized EDC. (c) Direct comparison of spectra below and above T_C.

from CDW fluctuations. Gap extracted through a spectra function fitting is plotted in Figure 5.6b, which can be fitted well with a pure d-wave like function. The maximum gap is around $\Delta = 8.8$ meV, much smaller than the on in $x = 0.4$ sample. The gap at the arc tip is around 6 meV, is exactly the same as observed by STM. A much larger weight transfer from low binding energy to high binding energy is clearly seen in $x = 0.1$ sample.

5.2.2 Temperature dependence of $\mathbf{La_{0.4}Bi_2Sr_{1.6}CuO_{6+\delta}}$

Detailed temperature dependence is shown in Figure 5.4a. Antinodal EDCs are symmetrized to remove the Fermi function, and then normalized to the EDC at 180K. A gap is clearly observed at T = 5K, as T goes above $T_C = 30$K, the gap persists and is filled in until $T^* \sim 150$K. The intensity at E_F becomes larger and the gap becomes larger as T increases. To quantitatively extracted the gap value, a Lorenz fit is performed on the spectra without a peak as shown in Figure 5.4a. The fitting parameter of Lorentz width is a good quantization of the gap. The gap opens at T^* as T goes below T_c, the gap value becomes smaller. This is the result of opening of SC gap and building of SC peaks we discussed earlier. This phenomenon has been shown in earlier results [7,8], but has not been discussed because of the effect is very weak. The temperature dependence of intensity at different binding energies is plotted in Figure 5.4b. The intensity at$\omega = 0$ meV goes monotonously up at T increases. But the intensity at $\omega = 5 \sim 20$ meV drops first and then goes up as T increases.

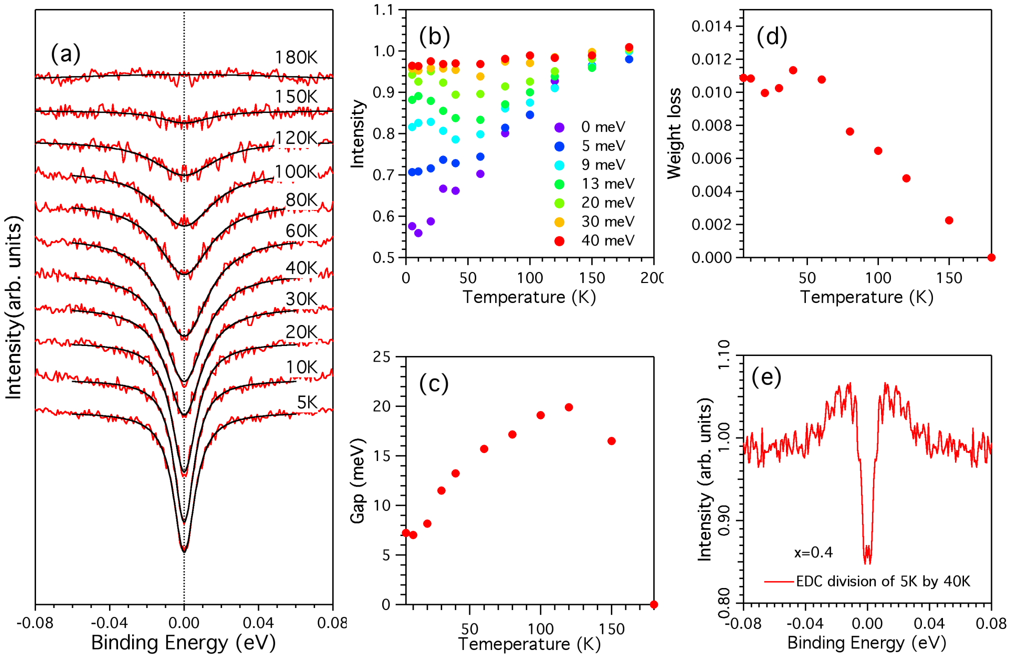

Figure 5.4: Temperature dependence of $La_{0.4}Bi_2Sr_{1.6}CuO_{6+\delta}$sample. (a) T dependence of spectra at antinodal region. The spectra is symmetrized and normalized to the one at 180K. The black line is a Lorentz fit. (b) The intensity at different binding energies. (c) T dependence of the antinodal gap. (d) T dependence of wight loss. (e) Spectral of 5K divided by 40K.

The superconducting gap energy is around 13 meV and spreads over a finite energy range. The weight loss is plotted in Figure 5.4d. The opening of the superconducting gap transfers weight from the low binding energy to the high binding energy, but the total weight is conserved. So the weight in Figure 5.4d is flat below T_C. However the incommensurate CDW gap does not conserve weight, we clearly see a decrease of weight at T increase. This different behavior in superconducting state and pseudo-gap gap state indicates the different nature of those two phases. Figure 5.5 shows the temperature dependence at the nodal region. Above T_C, the nodal region gap closes

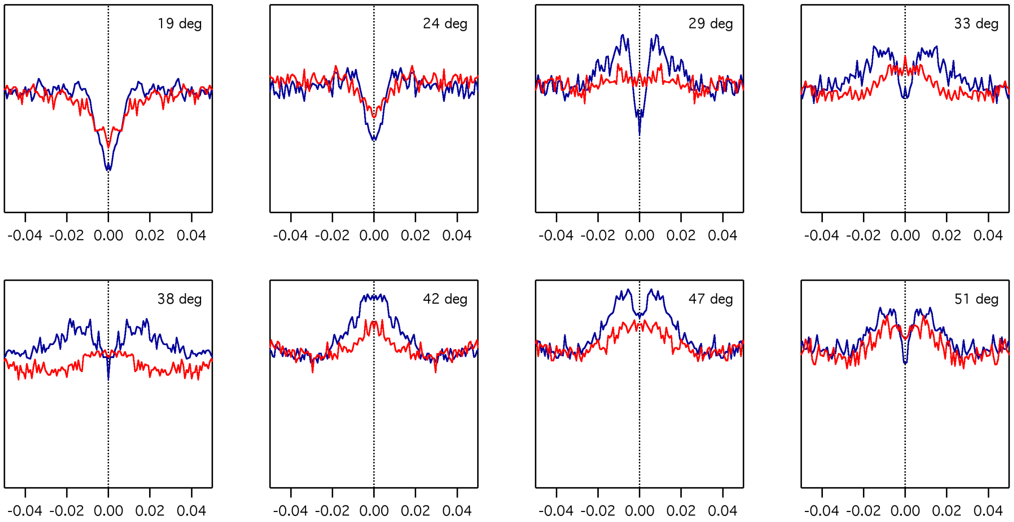

Figure 5.5: Temperature dependence at the nodal region of $La_{0.4}Bi_2Sr_{1.6}CuO_{6+\delta}$sample. Blue line is measured at 10K, red line is measured at 45K. The angle is the Fermi surface angle, 0 degree is the (0,π) direction, 45 is the (π, π) direction.

at T_C, but the antinodal region gap persists above T_C.

5.2.3 Pseudogap in overdoped $La_{0.1}Bi_2Sr_{1.9}CuO_{6+\delta}$

$La_{0.1}Bi_2Sr_{1.9}CuO_{6+\delta}$with Tc=18K is an overdoped sample. This can be seen from resistivity data and confirmed by the Fermi surface mapping. Detailed T dependence has performed at the antinodal region, as shown in Figure 5.6a. A pseudogap is observed with $T^* = 70$ K, which is quite high considering the high doping level and $T_C = 18$ K. The gap extracted by a spectral function fitting is plotted vs T

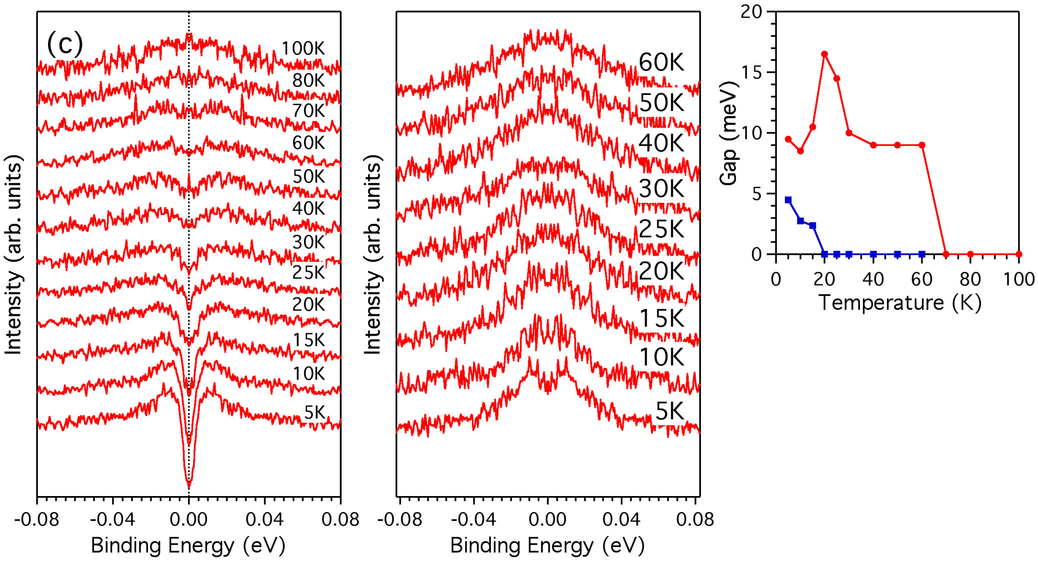

Figure 5.6: Temperature dependence of $La_{0.1}Bi_2Sr_{1.9}CuO_{6+\delta}$sample. (a) T dependence at the antinodal region.(b) T dependence at the intermediate region between the nodal and antinodal region. (c) Gap evolution with T from (a) and (b). The ARPES spectra is symmetrized EDC to remove the Fermi function.

in Figure 5.6c. As T goes above T_C, gap increases a little bit and then decreases. The unusual T dependence could be a result of two competing phases. The T dependence around point B, shown in the inset shows a smaller gap, the gap decreases monotonously as T increases and close at T_C. So the picture is clear, below T^*, pseudogap opens at the antinodal region, form a Fermi arc. As T goes below T_C, superconducting gap opens at both the nodal and antinodal region. At the nodal region, the SC gap opens at E_F. However at the antinodal region, the SC gap opens on top of the pseudogap. The temperature dependence at point B clearly shows a closing nature of the gap. The gap becomes smaller as T increases and closes at T_C.

5.3 Particle hole asymmetry

The symmetrization of EDC can be done at k_F assuming particle-hole symmetry. A more rigorous way to probe the state above E_F is by dividing the Fermi function convoluted with resolution function [16]. This process can be done only with high resolution data and good signal noise ratio. The data above T^* shows symmetrized spectra about the $\omega = 0$ meV. But between the temperature range 40∼150K, the intensity above E_F is very different from those below E_F. The particle-hole asymmetry is a signature of of CDW or (SDW). Below T_C, the spectra becomes symmetry again, reflecting the particle-hole symmetry nature of superconductivity [8, 17]. This particle-hole asymmetry can be also seen in sample $La_{0.1}Bi_2Sr_{1.9}CuO_{6+\delta}$as shown in Figure 5.8.

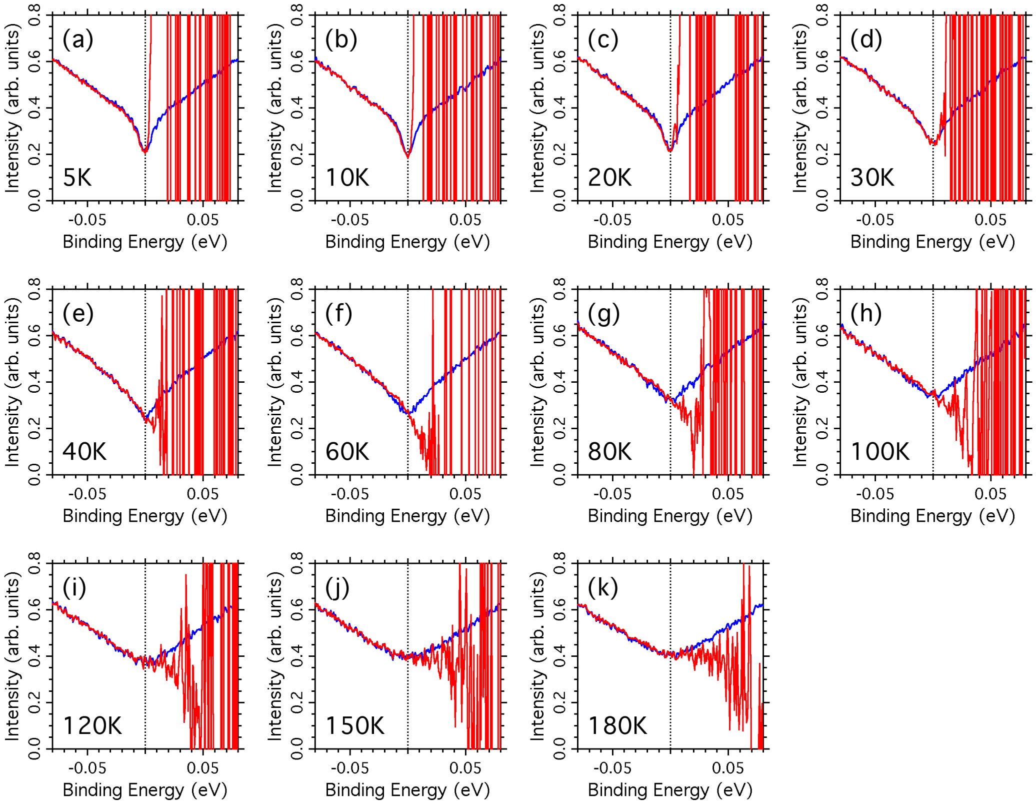

Figure 5.7: Fermi surface division at different temperature of $La_{0.4}Bi_2Sr_{1.6}CuO_{6+\delta}$. The blue line is the symmetrized EDC. The red line is the spectra of EDC divided by the Fermi function convoluted with resolution function.

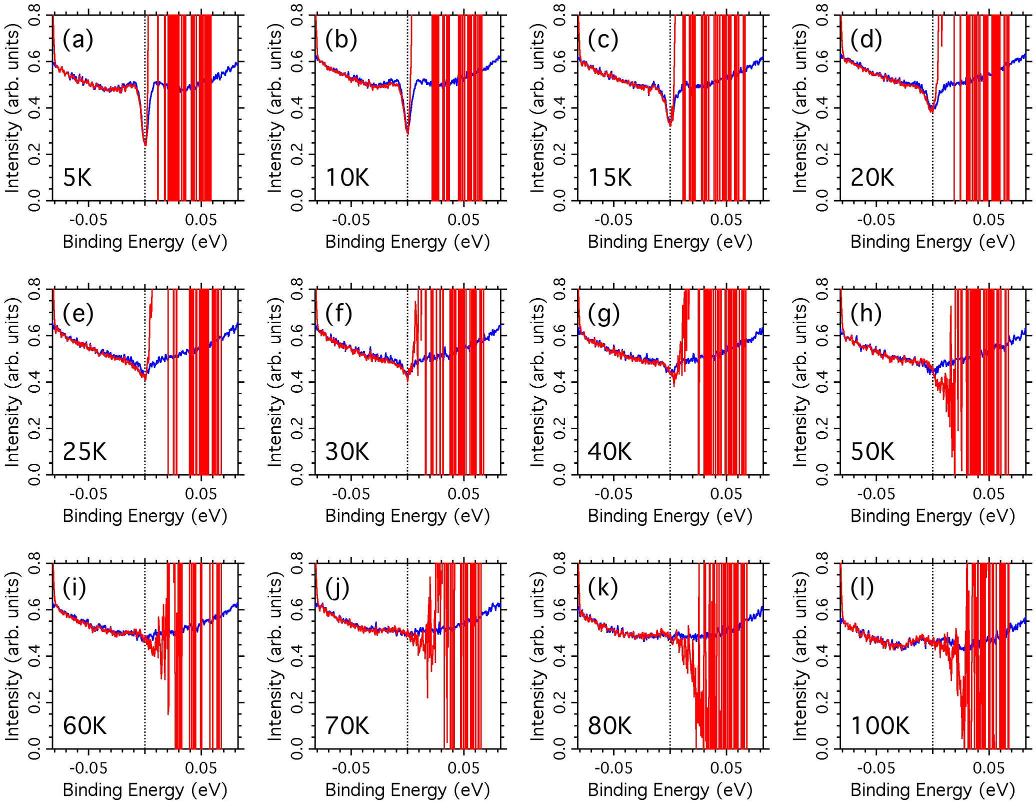

Figure 5.8: Fermi surface division at different temperatures of $La_{0.1}Bi_2Sr_{1.9}CuO_{6+\delta}$. The blue line is the symmetrized EDC. The red line is the spectra of EDC divided by the Fermi function convoluted with the resolution function.

5.4 Superconducting gap

With the resolving of superconducting gap in $La_xBi_2Sr_{2-x}CuO_{6+\delta}$. We plot the T_C versus superconducting gap in Figure 5.9 for materials $Bi_2Sr_2CaCu_2O_{8+\delta}$, $La_xBi_2Sr_{2-x}CuO_{6+\delta}$, $Bi_xBi_2Sr_{2-x}CuO_{6+\delta}$. At optimally doping, T_C scales linearly with the gap value.

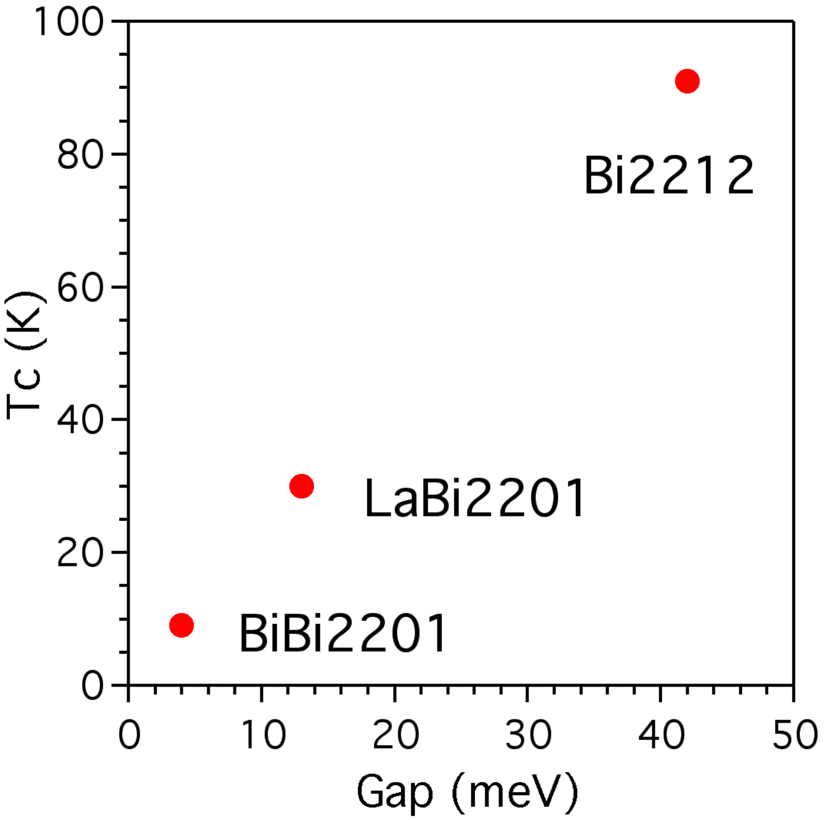

Figure 5.9: Correlation of T_C with superconducting gap in different materials.

5.5 Discussion

We observed two gaps coexisting in $La_{0.4}Bi_2Sr_{1.6}CuO_{6+\delta}$. The large pseudogap is associated to CDW, the small gap is attributed to superconductivity. CDW is one of many explanations for the pseudogap and there is possibility that the CDW occurs only at surface. The coexisting of two gaps rule out the the observed large gap is caused by fluctuating pairing gap. Our data do not rule out the possibility of an additional pseudogap related to pair fluctuation existing in a narrow temperature range above T_C. In summary a pseudogap above T_C and two gaps coexisting below T_C is observed in $La_xBi_2Sr_{2-x}CuO_{6+\delta}$, and the pseudogap extends to the over-doped regime.

Bibliography

[1] A. G. Loeser et al., Science **273**, 325 (1996).

[2] H. Ding et al., Nature **382**, 51 (1996).

[3] P. A. Lee et al., Rev. Mod. Phys. **78**, 17 (2006).

[4] M. R. Norman et al., Phys. Rev. B **76** 174501 (2007).

[5] A. Kanigel et al., Phys. Rev. Lett. **99**, 157001 (2007).

[6] K. Tanaka et al., Science **314**, 1910 (2006).

[7] T. Kondo et al., Phys. Rev. Lett. **98**, 267004 (2007).

[8] W. Lee et al., Nature **450**, 6219 (2007).

[9] M. R. Norman et al., Phys. Rev. B **57** R11093 (1998).

[10] J. Wei et al., arXiv:0801.2212 (2008).

[11] J. M et al., arXiv:0807.3294 (2008).

[12] Y. Kohsaka et al., Science **315**, 1380 (2007).

[13] T. Hanaguri et al., Nature **430**, 1001 (2004).

[14] W. D. Wise et al., arxiv:0806.0203 (2008).

[15] H. Ding et al., Phys. Rev. Lett. **87**, 227001 (2001).

[16] H. B. Yang et al., presentation at APS March meeting (2008).

[17] H. Matsui et al., Phys. Rev. Lett. **90**, 217002 (2003).

[18] L. Ren et al., arXiv: